Feedback Control of a Superconducting Qubit

Thomas Michael Karg

Bachelor's thesis
ETH Zürich

Supervisors:
Yves Salathé, Christopher Eichler and Prof. Andreas Wallraff

February 13, 2013

Abstract

We report about a discrete feedback protocol to control a superconducting transmon qubit in the σ_z basis. In the first step the qubit is projectively measured via the dispersive phase shift of a coherent microwave tone transmitted through a capacitively coupled coplanar waveguide resonator. Successive single shot read out with 80% fidelity is enabled by means of a Josephson parametric amplifier operated in the phase sensitive mode. The resonator output is processed on a field programmable gate array (FPGA). From the linearly filtered homodyne signal we infer the qubit state based on a threshold mechanism. Given that measurement result we are able to trigger a π pulse resonant with the qubit $e \leftrightarrow g$ transition conditioned on either ground (g) or excited state (e).

Tailored to the feedback scheme and in order to better analyze single-shot read out data a novel histogram application for the FPGA has been designed. We are able to record time resolved histograms of the resonator output field and directly correlate measured histograms before and after feedback.

With a qubit relaxation time of $\simeq$ 940 ns and a delay of 400 ns between state preparation and feedback operation errors due to qubit decay play a substantial role. The feedback delay is composed of the time to achieve maximal discrimination of the qubit states (150 ns) and signal processing on the FPGA (250 ns). Despite this drawback we achieve state fidelities of 80% for the ground state and 72% for the excited state with the corresponding feedback schemes.

Contents

Chapter 1

Introduction

Quantum information processing is a rapidly emerging field in physical science. As the name suggests, quantum mechanical systems are studied regarding their properties of storing and processing information. However, in a real experimental setup, these systems are never purely quantum. This leads to some undesired phenomena like relaxation and decoherence. On the contrary, coupling to a classical system is also a topic of primary interest in the context of quantum measurement and feedback control. While dissipation is closely related to information loss, collecting that information and feeding it back into the system can be used as a tool to deterministically steer quantum dynamics [Wiseman, 1994].

As opposed to open-loop control where coherent operations are scheduled beforehand, closed-loop or feedback control depends on the real-time acquisition of information about the system [Lloyd, 2000]. This opens up a variety of new possibilities for coherent control. These include adaptive measurement [Armen et al., 2002], continuous quantum error correction [Ahn et al., 2002], feedback cooling [Steixner et al., 2005], stabilization of Fock states in an optical cavity [Sayrin et al., 2011], maintaining Rabi oscillations in a superconducting qubit [Vijay et al., 2012] and stabilization of pure states of a two level atom [Wang and Wiseman, 2001; Risté et al., 2012a].

Measurement in quantum mechanics is a particularly delicate topic due to its projective and stochastic nature [Wiseman and Milburn, 2009]. The strength of a measurement is not only a measure for the rate at which information is extracted from the system, but also determines the speed of decoherence, that is the emergence of classicality. For the purpose of feedback the choice is between strong measurement with discrete feedback operation and weak measurement with continuous feedback [Doherty et al., 2001]. In this thesis the latter approach has been pursued, partly because it is more tractable and also due to the prospect of future

applications to fill gaps in open loop control.

That motivation is best explained in the context of the experimental architecture used in this thesis, circuit Quantum Electrodynamics [Wallraff et al., 2004; Blais et al., 2007]. Quantum information processing with superconducting circuits and microwave photons has been extensively studied and refined for open-loop applications [Eichler et al., 2012b; Fedorov et al., 2012; Baur et al., 2012; Steffen et al., 2012]. In particular high fidelity single shot read out [Vijay et al., 2011] by means of parametric amplification [Yurke and Buks, 2006] offers direct application of discrete feedback control in quantum error correction and quantum teleportation [Bennett et al., 1993]. Quantum teleportation features a Bell basis measurement with four possible outcomes each of which giving rise to another qubit rotation that retrieves the teleported state from the corresponding post-measurement state. The feedback scheme designed here handles only binary decisions but may be regarded as a first step towards an implementation of the full solution.

This thesis is structured as follows. In the subsequent second chapter, a review of circuit quantum electrodynamics is given. Particular emphasis is laid on the dispersive interaction of a single qubit with a capacitively coupled resonator. This interaction allows one to perform a quantum non demolition measurement of the qubit state via homodyne detection of the resonator output. Moreover the concept of parametric amplification is introduced as a tool for nearly quantum-limited amplification.
Afterwards, in chapter three, the notion of feedback control in quantum mechanics is discussed. This thesis is concerned with discrete feedback operations conditioned on information extracted from a previous measurement record. Next to quantum measurement theory this involves linear or nonlinear (Bayesian) filtering in order to make an optimal estimate for the qubit state.
The fourth chapter gives account of the experimental setup and the digital signal processing hardware that were used to establish a discrete feedback scheme of a single transmon qubit. Signal processing encompasses both the feedback loop and data acquisition.
First results obtained with this apparatus are presented and analyzed in chapter five. The thesis ends with a conclusion in chapter six.

Chapter 2

Circuit Quantum Electrodynamics

The study of the interaction between light and matter on the atom – photon level is known as *Cavity Quantum Electrodynamics* (QED) [Walls and Milburn, 2008; Cohen-Tannoudji et al., 1998]. Usually, quantum coherence is established on microscopic degrees of freedom such as photons, ions or spins. Contrarily, *Circuit Quantum Electrodynamics* [Wallraff et al., 2004; Blais et al., 2004] is a mesoscopic scale technique with superconducting artificial atoms coupled to electromagnetic field modes of a microwave resonator. The system is realized as an integrated circuit placed on a chip. This is deemed to be a promising scheme for quantum information processing [Devoret et al., 2007] due to high coupling efficiency, tunable resonances and scalability. Quantum bits (qubits) are realized in the subsystem of ground and first excited state of the atom. Coherent control and read-out is implemented by applying narrow-bandwidth microwave frequency tones to either qubit or resonator.

The essential nonlinearity for artificial atom design is provided by Josephson junctions. Macroscopic quantum coherence requires ultra-low dissipation and noise which is achieved by superconducting materials operated at extremely low temperatures in the milli-Kelvin (mK) range. In the measurements presented in this thesis, a charge-insensitive transmon qubit design was used [Koch et al., 2007].

2.1 Qubit-resonator dynamics

The joint system of a two-level system coupled to a single mode of an electromagnetic field is well-described by the Jaynes-Cummings model [Cohen-Tannoudji et al., 1998; Walls and Milburn, 2008]. For a qubit with transition frequency ω_a, a resonator mode with resonance frequency ω_r and atom-field coupling strength g

we have the hamiltonian

$$H = \hbar\omega_r \left(a^\dagger a + \frac{1}{2}\right) + \frac{1}{2}\hbar\omega_a\sigma^z + \hbar g\left(a + a^\dagger\right)\sigma^x \ . \tag{2.1}$$

Here, a and $a^\dagger$ are the annihilation and creation operators of the resonator mode, the σ^i are the Pauli matrices in the Hilbert space of the qubit. External sources of radiation are modeled with interaction terms

$$H_d^r = a\ \varepsilon_d(t)e^{i\omega_d t} + a^\dagger\ \varepsilon_d^*(t)e^{-i\omega_d t}$$

for the resonator and

$$H_d^a = \sigma^-\ \varepsilon_d(t)e^{i\omega_d t} + \sigma^+\ \varepsilon_d^*(t)e^{-i\omega_d t}$$

for the qubit. In both cases $\varepsilon(t)$ is the drive field pulse envelope and ω_d is the carrier frequency. $\sigma^\pm$ are the raising and lowering operators for the qubit effecting the transitions $g \leftrightarrow e$ between the ground (g) and excited (e) state of the qubit. Typically ω_d is chosen to match the transition frequency of either system such that in the terms become stationary in the interaction frame.

If qubit and resonator are tuned into resonance ($\omega_a \approx \omega_r$), then the eigenstates of the Jaynes-Cummings Hamiltonian 2.1 are dressed states [Cohen-Tannoudji et al., 1998]. In this case it is impossible to distinguish between qubit and resonator. From a quantum information perspective, however, it is of particular interest to keep them separated. Otherwise coherent control of a single subsystem and quantum nondemolition measurement (QND) would not be feasible. Thus in the following we will be concerned with the *dispersive regime* characterized by qubit-resonator detunings $\Delta = \omega_a - \omega_r$ being much larger than the coupling strength g: $g/\Delta \ll 1$. The dispersive Hamiltonian can be obtained from a transformation of the Hamiltonian 2.1 with the unitary $U = \exp(\frac{g}{\Delta}(a^\dagger\sigma^- - a\sigma^+))$. Keeping only linear order in $\frac{g}{\Delta}$ this yields [Blais et al., 2004]

$$\begin{aligned} \tilde{H} = UHU^\dagger &= \hbar\Big(\omega_r + \chi\sigma^z\Big)a^\dagger a \ + \ \frac{\hbar}{2}(\omega_a + \chi)\sigma^z && (2.2)\\ &= \hbar\omega_r a^\dagger a \ + \ \frac{\hbar}{2}\left(\omega_a + 2\chi\left(a^\dagger a + \frac{1}{2}\right)\right)\sigma^z && (2.3)\end{aligned}$$

Here, the dispersive shift for a pure two level atom would be $\chi = g^2/\Delta$. For the transmon qubit which also features higher excited states, accurate calculations yield an effective dispersive shift of [Koch et al., 2007]

$$\chi = \frac{g^2 E_C}{\Delta(E_C - \Delta)}. \tag{2.4}$$

Here, E_C is the charging energy of the transmon which approximately corresponds to the anharmonicity between first and second excited state. The dispersive shift χ arises as both a qubit state dependent frequency pull on the resonator (2.2) and photon number splitting of the qubit frequency (2.3) [Gambetta et al., 2006]. In the case that number splitting cannot be resolved in spectroscopy due to large natural linewidth of the qubit, only an average shift $\propto 2\langle n\rangle\chi$ is observed, called the a.c. Stark shift. We see that in the dispersive limit, the Hamiltonian is approximately diagonal in the uncoupled basis $\{|g,n\rangle, |e,n\rangle\}_n$. It is important to note, however, that this approximation breaks down for large numbers of photons $\langle n\rangle$ populating the resonator. The scale is defined by the critical photon number $n_{crit} = \Delta^2/4g^2$ such that the necessary condition for the dispersive approximation becomes $\langle n\rangle \ll n_{crit}$.

In the absence of decoherence, or for a closed quantum system, the time evolution of the density matrix is given by the Liouville - von Neumann equation

$$i\hbar\frac{\mathrm{d}\,\rho}{\mathrm{d}\,t} = [H,\rho]. \tag{2.5}$$

Moving to a rotating frame with unitary propagator U induces the following transformations for operators A or density matrices ρ in the Schrödinger picture:

$$\tilde{A} = U^\dagger A U\ , \quad \tilde{\rho} = U^\dagger \rho U. \tag{2.6}$$

Choosing an exponential representation $U = \exp(-itF/\hbar)$ with self-adjoint F yields the following time evolution for $\tilde{\rho}$:

$$i\hbar\frac{\mathrm{d}\,\tilde{\rho}}{\mathrm{d}\,t} = \left[\tilde{H} - F,\ \tilde{\rho}\right]. \tag{2.7}$$

Choosing F appropriately can lead to a dramatic simplification of the equations of motion because only interaction terms need to be considered.

In an open quantum system, coupling to a classical environment gives rise to decoherence. In the limit where all information transferred to the environment is irreversibly lost the system dynamics can be modeled by a Markovian master equation [Lindblad, 1976]. For the qubit-resonator system, it has the form [Walls and Milburn, 2008]

$$\frac{\mathrm{d}\,\rho}{\mathrm{d}\,t} = -\frac{i}{\hbar}[H,\rho] + \kappa\mathcal{D}[a]\rho + \gamma_1\mathcal{D}[\sigma_-]\rho + \frac{\gamma_\phi}{2}\mathcal{D}[\sigma_z]\rho = \mathcal{L}\rho. \tag{2.8}$$

Here $\gamma_1 = 2\pi/T_1$ is the qubit's relaxation rate with relaxation time T_1, γ_ϕ is its pure dephasing rate such that qubit decoherence amounts to $\gamma_2 = \gamma_1/2 + \gamma_\phi = 2\pi/T_2$ with decoherence time T_2. Decay from the resonator occurs at the rate κ. The total Hamiltonian including drives is denoted H and $\mathcal{D}[X]\rho = X\rho X^\dagger - \{X^\dagger X, \rho\}/2$ is the Lindblad superoperator. The total time evolution is captured by the Liouvillian superoperator $\mathcal{L}$.

2.2 Cavity-Bloch equations in the dispersive regime

The main advantage of the dispersive regime is that resonator and qubit are essentially decoupled. This is reflected in the fact that σ^z and $a^\dagger a$ commute with the dispersive Hamiltonian and are thus both constants of the motion. This allows to perform a QND measurement of the qubit state in the $(|e\rangle, |g\rangle)$ basis by measuring the phase shift of the resonator transmission [Bianchetti et al., 2009]

$$s(t) = \sqrt{Z\hbar\omega_r\kappa}\,\langle a(t)\rangle \tag{2.9}$$

which can be derived by input-output theory [Gardiner and Collett, 1985]. Here Z is the characteristic impedance of the transmission line capacitively coupled to the resonator. In practice, the quadrature components $I(t) = \Re s(t)$ and $Q = \Im s(t)$ of the resonator transmission are determined after heterodyne detection with a local oscillator at frequency $\omega_{LO} = \omega_r - \omega_{IF}$ and phase φ_{LO}. The intermediate frequency ω_{IF} is typically 25 MHz which matches the bandwidth of subsequent signal processing electronics (100 MHz). The quadratures are then computed as

$$\begin{aligned} I(t) &= \cos(\omega_{IF}t)\,\Re\left\{s(t)e^{-i\omega_{LO}t+i\varphi_{LO}}\right\}, \\ Q(t) &= \sin(\omega_{IF}t)\,\Re\left\{s(t)e^{-i\omega_{LO}t+i\varphi_{LO}}\right\}. \end{aligned} \tag{2.10}$$

If a is treated as a Heisenberg observable, the quantum Langevin equation describing its time evolution subject to an input mode b_{in} is [Gardiner and Collett, 1985]

$$\frac{\mathrm{d}\,a}{\mathrm{d}\,t} = -i(\omega + \chi\sigma_z)a - \frac{\kappa}{2}a + \sqrt{\kappa}b_{in} \tag{2.11}$$

We consider the input to be a coherent measurement tone with amplitude $\varepsilon_m(t)$ and transform to a rotating frame at its carrier frequency ω_m. By displacing the cavity mode in the vacuum state to a coherent state $|\alpha\rangle$, we obtain the equation of motion

$$\frac{\mathrm{d}\,\alpha}{\mathrm{d}\,t} = -i\left(\Delta_{rm} + \chi\sigma_z\right)\alpha - \frac{\kappa}{2}\alpha - i\varepsilon_m \tag{2.12}$$

Here $\Delta_{rm} = \omega_r - \omega_m$ is the detuning between the bare resonator (in the absence of a qubit) and the measurement tone. In the context of single-shot read-out by strong, projective measurement, the qubit polarization σ_z follows a stochastic evolution, jumping between ± 1 each time the qubit decays or is excited. The latter is negligible at moderate measurement powers and low thermal noise. Qubit decay, however, occurs at the rate γ_1 which implies that decay times τ_d are exponentially distributed such that for an initially $(t = 0)$ excited state

$$\sigma_z(t) = \begin{cases} 1 & t < \tau_d \\ -1 & t \geq \tau_d \end{cases} \tag{2.13}$$

Each discrete value of σ_z gives rise to another coherent state of the resonator mode via the equation of motion 2.12. Due to their characteristic frequency shift $\chi\sigma_z$ they encode the qubit state and are thus called *pointer states* $\alpha_\pm$ [Walls and Milburn, 2008]. Entanglement of the qubit state with such pointer states of the transient field [Gambetta et al., 2008] enables indirect measurement of the qubit as will be explained in Section 3.2. The solution of equation 2.12 is obtained formally by Fourier transformation (indicated by $\mathcal{F}$ or $\widehat{\ }$)

$$\alpha(t) = \mathcal{F}^{-1}\left[\frac{\hat{\varepsilon}_m(\omega)}{i\frac{\kappa}{2} - (\omega + \Delta + \chi\sigma_z)}\right](t) \tag{2.14}$$

$$= -i\sqrt{2\pi}\left(\varepsilon_m(t') * e^{(-i(\Delta+\chi\sigma_z)-\frac{\kappa}{2})t'}\right)(t) \tag{2.15}$$

In the second line we have rewritten the inverse Fourier transformation as a convolution integral of the measurement pulse envelope with a Lorenzian filter of bandwidth κ and centered at $\Delta + \chi\sigma_z$. In the context of measuring the qubit state via entanglement with the resonator field, κ also determines the rate at which information about the qubit state leaves the cavity. Effectively, we are interested in the steady state (s) solution which corresponds to maximal information about the qubit state:

$$\alpha^s_\pm(t) = \varepsilon_m(t)\,\frac{(\Delta \pm \chi) + i\frac{\kappa}{2}}{(\Delta \pm \chi)^2 + (\frac{\kappa}{2})^2} \tag{2.16}$$

For zero detuning the distinguishability between ground and excited state response is maximal and amounts to

$$\alpha^s_+(t) - \alpha^s_-(t) = \frac{2\chi\varepsilon_m(t)}{\chi^2 + (\frac{\kappa}{2})^2} \tag{2.17}$$

which is real valued. Moreover the steady-state angles of the pointer states with respect to the Q axis are

$$\theta_\pm = \mathrm{Arg}(-i\alpha^s_\pm) = \pm\arctan\left(\frac{2\chi}{\kappa}\right). \tag{2.18}$$

We see that all information about the qubit state is actually stored in the phase of the transient photon field. Equation 2.17 tells us, that by applying an appropriate local oscillator phase in heterodyne detection, it is possible to rotate the entire state information into a single quadrature. However due to phase noise this will be possible only approximately. That information is stored in a single quadrature is a necessary condition for the application of a parametric amplifier in the phase-sensitive mode. There, one quadrature is amplified while the other is attenuated. As we will see in the next section, this allows in principle to avoid adding noise in the amplification process.

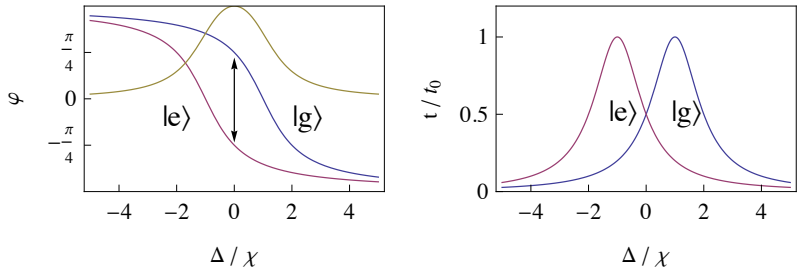

Figure 2.1: This plot shows the resonator transmission in phase (left) and amplitude (right) as a function of the detuning Δ of the measurement tone from the bare resonator frequency ω_r. Blue and red curves correspond to the qubit in the ground and excited state, respectively. At zero detuning state information is maximal and stored in the phase shift only.

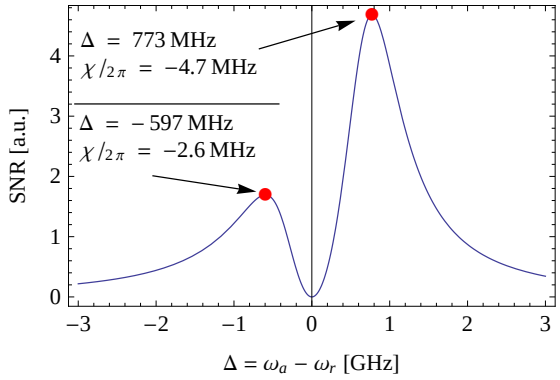

Figure 2.2: Here, a plot of the steady state SNR from Equation 2.19 versus qubit-resonator detuning $\Delta = \omega_a - \omega_r$ is shown. The calculation assumes the parameters $g/2\pi = 65$ MHz, $E_c/\hbar = 341$ MHz and $\kappa/2\pi = 6.45$ MHz which are characteristic of the setup used for this thesis. Even though SNR is much smaller for negative detunings this position might nonetheless be favorable because of enhanced T_1.

For a constant measurement tone, the signal to noise ratio for qubit state discrimination is given by [Gambetta et al., 2008]

$$SNR \propto \frac{n\kappa\chi^2 T_1}{\chi^2 + \kappa^2/4}, \tag{2.19}$$

where n is the average photon number in the resonator during measurement. By fixing the ratio $n_{crit}/n \propto \Delta^2 \gg 1$ and using Equation 2.4 for χ it is possible to maximize the SNR as a function of the qubit-resonator detuning Δ (see Figure 2.2. Moreover, for small detunings T_1 is limited by the Purcell rate [Purcell, 1946]. Another important aspect is the speed of information acquisition $\Gamma_m(t) \propto \kappa|\alpha_e(t) - \alpha_g(t)|^2$ [Gambetta et al., 2008]. As Govenius [2012] pointed out, the property $\Re(\alpha_e(t) - \alpha_g(t))$ increases only quadratically in time at the measurement onset.

Creating nonzero initial population in the resonator could reduce this to linear time dependence. For this reason an on-hold measurement pulse has been designed that starts with a short, strong on-pulse followed by a moderate steady state hold-pulse. The dimensionless amplitude ratio between both is $r = \varepsilon_{on}/\varepsilon_{hold} \propto \sqrt{\chi^2 + \kappa^2/4}/t_{on}$ and of the order 10. The duration of the on-pulse is denoted t_{on}. Another pulse shape seems natural, namely an exponential decaying one with time constant $\lambda = 1/t_{on}$ such that the steady state value is the hold measurement amplitude. With θ denoting the Heaviside theta function the pulse shapes are

$$\begin{aligned} \varepsilon_{on-hold}(t) &= \theta(t - t_{on}) + r\big(\theta(t) - \theta(t - t_{on})\big), \\ \varepsilon_{exp}(t) &= \theta(t)\left(1 + re^{-t/t_{on}}\right). \end{aligned}$$

The effect of all three different pulse shapes are plotted in Figure 2.3 for the amplitudes and Figure 2.4 for the powers or photon number equivalents. We see that the exponential pulse leads to slightly better discrimination between ground and excited states. Moreover Figure 2.5 suggests that it pumps slightly less photons into the resonator than the on-hold pulse which makes it more compatible with the criticality condition $\langle n \rangle \ll n_{crit}$. However it is not clear how low pass filtering of the measurement tone in the course of pulse generation and propagation influences this effect. For this thesis step and on-hold measurement pulses were employed.

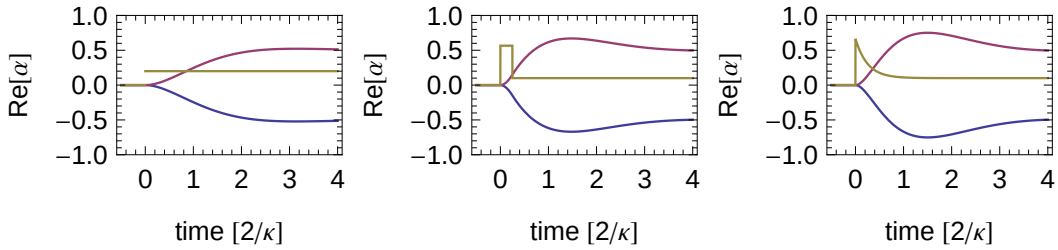

Figure 2.3: Real parts of the solutions to the cavity Bloch equations for the three different measurement pulses step function (left), on-hold (middle) and exponential decaying pulse (right). The ground and excited state responses are drawn in blue and red, respectively, the pulse shape is indicated in yellow. The parameters are $\kappa = 2\chi$, $t_{on} = 1/2\kappa$ and $r = 4\sqrt{2}$.

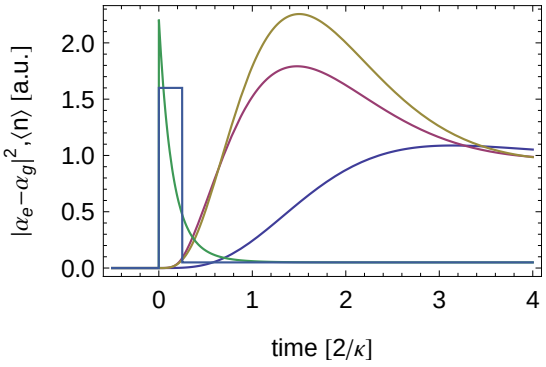

Figure 2.4: Square distances $|\alpha_e - \alpha_g|^2$ of the solutions to the cavity Bloch equations for the three different measurement pulses step function (blue), on-hold (red) and exponential decaying pulse (yellow). The pulse powers which are proportional to the cavity photon number are shown in the respective colors.

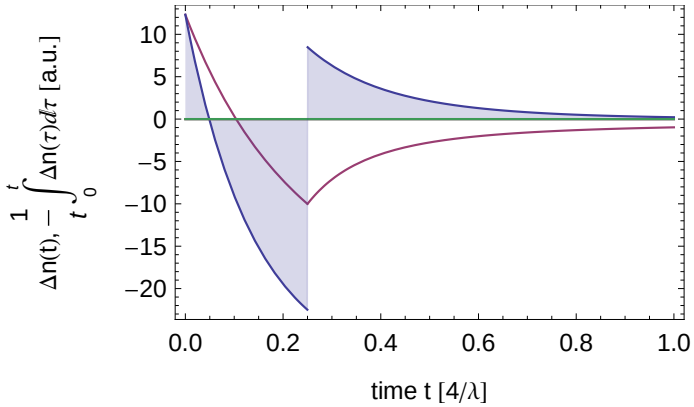

Figure 2.5: Difference (blue) and mean integrated difference (red) between the measurement powers of exponentially decaying and on-hold pulse: $\Delta n = n_{exp} - n_{on-hold}$. Here, $\lambda = 1/t_{on}$.

2.3 Parametric amplification

QND measurement of a superconducting qubit via dispersive read-out is constrained by low measurement power [Boissonneault et al., 2009]. However, a signal power corresponding to a single photon is not macroscopically detectable by commercial amplifiers which on average add an order of magnitude more noise photons. For high-fidelity single-shot read-out, however, it is indispensable to achieve a high signal-to-noise ratio (SNR). Close to quantum-limited [Caves, 1982] amplification can instead be achieved by drawing upon the qualities of parametric amplifiers. Relying on nonlinearities, these have proven to be a valuable tool for detecting quantum dynamics on the single-photon level such as quantum jumps [Vijay et al., 2011].

The quantum limit on bosonic amplifiers can in principle be understood by considering a field mode a with quadrature components X and P

$$X = X_\varphi = \frac{1}{\sqrt{2}}\left(ae^{-i\varphi} + a^\dagger e^{i\varphi}\right) \ , \quad P = P_\varphi = -\frac{i}{\sqrt{2}}\left(ae^{-i\varphi} - a^\dagger e^{i\varphi}\right). \tag{2.20}$$

We have $[a, a^\dagger] = 1$ or equivalently $[X_\varphi, P_\varphi] = i \ \forall\varphi$. The phase φ is kept here because in homodyne or heterodyne detection it can be adjusted as the phase of the LO signal. An amplification process is called *phase-preserving* (or phase-insensitive) if the gain is independent of the phase φ, i.e. both quadratures are amplified equally. Naively, one could write $X \mapsto \sqrt{G}X$, $P \mapsto \sqrt{G}P$ where G is the power gain. However, in order to preserve the canonical commution relations the amplified mode b must contain a bosonic noise mode f that is uncorrelated with a, i.e. $b = \sqrt{G}a + \sqrt{G-1}f^\dagger$. Recognizing that f is in a vacuum state leads to the standard quantum limit that phase-preserving amplifiers add at least half a noise photon to the input signal [Clerk et al., 2010]. Phase preserving amplification near the quantum limit has been demonstrated experimentally by Bergeal et al. [2010].

Evading this quantum limit is possible if the amplifier is operated in the *phase sensitive* mode. In that case the quadrature components are treated differently, i.e. gain becomes a function of the quadrature phase φ. Ideally, this would look like $X \mapsto \sqrt{G}X$, $P \mapsto P/\sqrt{G}$. By amplifying one quadrature and attenuating the other the quadrature commutation relations $[X, P] = i$ are automatically maintained and, in principle, there need not be added noise (see Figure 2.6). It is crucial to note that $X = X_\varphi$ and $P = P_\varphi$ depend on the relative phase φ between pump and signal which has to be calibrated appropriately in order to have all information in the correct quadrature.

In practice, parametric amplifiers are realized by nonlinearly coupling the input

mode with a strong, classical pump. A cavity exhibiting a Kerr nonlinearity [Yurke and Buks, 2006] provides a good model for that situation:

$$H = \hbar\omega_0 A^\dagger A + \hbar K A^\dagger A^\dagger A A$$

where K is the Kerr constant and ω_0 the cavity resonance frequency. Then the conditions for parametric amplification can be derived from input output relations [Gardiner and Collett, 1985] for signal and pump coupled to the paramp:

$$a_{out} - a_{in} = \sqrt{\kappa} A$$

Here, the cavity decay rate is κ and $a = b_{signal} + b_{pump}$ is the joint input/output mode of the paramp. The nonlinear equations of motion of the intra-cavity mode A and signal and pump input mode a_{in} are

$$\frac{\mathrm{d}\,A}{\mathrm{d}\,t} = -i\omega_0 A - iKA^\dagger AA + \sqrt{\kappa} a_{in} + \text{dissipation} \tag{2.21}$$

$$\frac{\mathrm{d}\,a_{in}}{\mathrm{d}\,t}(\omega) = -i\omega a_{in}(\omega) + \sqrt{\kappa} A \tag{2.22}$$

An alternative way to think about parametric amplification is in terms of resonant scattering [Clerk et al., 2010] where energy from the pump mode is converted to energy of the signal mode. Phase sensitive amplification is realized by choosing the carrier frequencies of signal and pump to be equal. Still, in order to amplify the right quadrature, the relative phase between pump and signal has to be adjusted.

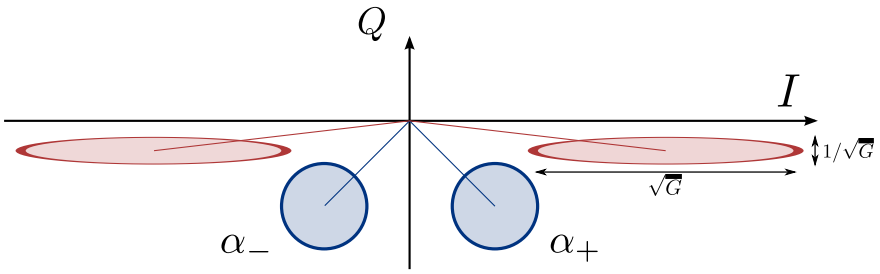

Figure 2.6: The effect of squeezing on the quadratures of the coherent pointer states $\alpha_\pm$ as produced by phase-sensitive amplification. The initial phase space distributions are painted blue, the squeezed, amplified distributions are shown in red. Here, the I quadrature is amplified by $\sqrt{G}$ and the Q quadrature by $1/\sqrt{G}$. This leads to a bigger separation $|\alpha_+ - \alpha_-|^2$ which is necessary for projection of the qubit onto $|e\rangle$ or $|g\rangle$.

2.4 Summary

Circuit QED has been introduced theoretically by discussing the dynamics of a single qubit-resonator system in the Jaynes-Cummings form. It has been shown that in the dispersive regime, with the transition frequencies of qubit and resonator largely detuned, the Hamiltonian is effectively diagonal in the uncoupled basis $\{|g,n\rangle, |e,n\rangle\}_n$. The interaction of both effects a qubit state-dependent frequency shift of the resonator which can be used to read-out the qubit state. For a coherent measurement tone on the bare resonator frequency, all information about the qubit will be contained in the phase (or single quadrature) of the transmitted field amplitude. This allows phase sensitive amplification near the quantum limit of added noise, a prerequisite for high-fidelity single-shot read-out. Parametric amplification offers a possible realization for that.

Chapter 3

Feedback control of quantum systems

3.1 Feedback in classical and quantum systems

Real physical systems often exhibit complex behaviour. In engineering, sophisticated feedback control schemes are required to ensure that machines operate properly. In classical physics, feedback, in its most general form, may be thought of as monitoring a system and using this information to apply certain forces that steer its dynamics into a desired direction. Thus the idea is to effect a particular kind of dynamics from a broad range of initial conditions. This may be illustrated in phase space. The state of a classical Hamiltonian system is fully characterized by a tuple of its generalized position and momentum coordinates. By steering the dynamics into the desired direction we mean that the region in phase space occupied by the system is transferred to another. This procedure may also need to contract phase volume because we do not admit the system to exhibt large deviations from a well defined dynamics. However, Liouville's theorem [Landau and Lifshitz, 1976] tells us that the phase volume in an autonomous Hamiltonian system is conserved. Therefore the system needs to be coupled to a controller system that "absorbs" excess phase volume via interaction potentials.

In a quantum mechanical system the situation is a bit more delicate. Classical observables which form a Poisson Algebra over the phase space are replaced by operators acting on a Hilbert space. Canonical commutation relations lead to the fact that measurement used to extract state information perturbs the system dynamics. For example the joint measurement precision of conjugate observables is finally limited by the Heisenberg uncertainty principle. Also, the dynamics of a continuously monitored quantum system will be strongly non-classical [Wiseman, 1994], e.g. it may exhibit quantum jumps corresponding to the observer's knowl-

edge about the system.
This leads to an alternative but equivalent conception which is to consider the state of a physical system instead of a set of observables. Classically, a physical system is described by a probability distribution over the outcomes of a measurement while the quantum analog is the density operator. In the course of measurement these quantities get updated according to the extracted information which is captured by stochastic differential equations [Doherty et al., 2000; Wiseman and Milburn, 2009] and also known as quantum filtering theory [Bouten et al., 2007]. Optimal control would require to solve these equations in real time which is a computationally hard problem such that linearized models or discretized versions are sought.

We may further distinguish between two alternatives for feedback control of quantum systems by choosing the control device to be of either classical or quantum mechanical nature [Lloyd, 2000].
Under *coherent quantum feedback* we understand that quantum information processing is used for producing the feedback [Lloyd, 2000; Nelson et al., 2000]. For example we may choose two copies of the same system, e.g. spins, and make them interact weakly via an additional degree of freedom, e.g. a vibrational mode [Cirac and Zoller, 1995]. Then it is possible to exchange the states of both spins by selective coherent operations on either spin. This method is effective in preserving quantum coherence and is reversible. Since it relies on creating entanglement between system and controller other mechanisms can be envisioned that exceed the capabilities of classical feedback.
Still it is possible to choose a *classical control* device. There, quantum state information is translated into classical bits. This requires measurement of the quantum system and is thus a stochastic process [Wiseman, 1994]. By projection onto the eigenstates of the measured observable coherence is irreversibly lost. Subsequent measurement outcome-dependent operations rely on the measurement being *quantum non-demolition* (QND). For this reason, measurement in the eigenbasis of the system Hamiltonian is required. Note that measurement in a realistic open system is not instantaneous but requires some time. Due to finite coupling strengths to some bath there will be relaxation and dephasing of the system and consequently lead to errors in the measurement and the feedback.

3.2 Theoretical description of measurement based feedback

This section gives a simple treatment of the quantum mechanics of measurement closely following reference [Wiseman and Milburn, 2009]. Consider the joint Hilbert space of the system S and an apparatus A, $\mathcal{H} = \mathcal{H}_S \otimes \mathcal{H}_A$. The apparatus serves as a meter or read-out device for the system. Before measurement, the system is in the initial state $\rho = \rho_S \otimes \rho_A$. There is no initial correlation between S and A. Moreover, the state of the apparatus is known to the observer. Now, time evolution of the joint system under the unitary operation $\hat{U}$ creates entanglement between S and A due to an interaction term in the Hamiltonian. Evolution for a delay τ leads to

$$\rho(t+\tau) = \hat{U}(\tau)\rho(t)\hat{U}^\dagger(\tau) = \hat{U}(\tau)\left(\rho_S(t) \otimes \rho_A(t)\right)\hat{U}^\dagger(\tau). \tag{3.1}$$

Then, a projective measurement of A with projection operators $\hat{\pi}_A(\lambda) = |\lambda\rangle_A\langle\lambda|$ is performed. The unnormalized post-measurement state for result λ is

$$\hat{\pi}_A(\lambda)\ \rho(t+\tau)\ \hat{\pi}_A^\dagger(\lambda) = \hat{M}_\lambda(\tau)\ \rho(t)\ \hat{M}_\lambda^\dagger(\tau) \tag{3.2}$$

with *measurement operators* defined as

$$\hat{M}_\lambda(\tau) = (\mathcal{I}_S \otimes \hat{\pi}_A(\lambda))\hat{U}(\tau). \tag{3.3}$$

We obtain the *conditional state* for a measurement result λ from

$$\rho_\lambda(t+\tau) = \frac{\hat{M}_\lambda\rho(t)\hat{M}_\lambda^\dagger}{\mathrm{Tr}\left(\hat{M}_\lambda\rho(t)\hat{M}_\lambda^\dagger\right)} = \frac{\mathcal{O}_\lambda\rho(t)}{\mathrm{Tr}\left(\rho(t)\hat{E}_\lambda\right)} = \frac{\mathcal{O}_\lambda\rho(t)}{\wp(\lambda)}. \tag{3.4}$$

with $\mathcal{O}_\lambda\rho = \hat{M}_\lambda\rho\hat{M}_\lambda^\dagger$ and probability operators $\hat{E}_\lambda = \hat{M}_\lambda^\dagger\hat{M}_\lambda$. The probability for the outcome λ is $\wp(\lambda) = \mathrm{Tr}\left(\rho\hat{E}_\lambda\right)$. The operations $\mathcal{O}_\lambda$ describe a general measurement on S by coupling to an apparatus A. They are linear, completely positive maps from the state space of $\mathcal{H}$ onto itself. Conservation of probability demands that

$$1 = \sum_\lambda \wp(\lambda) = \sum_\lambda \mathrm{Tr}(\mathcal{O}_\lambda\rho) = \mathrm{Tr}\left(\rho\sum_\lambda \hat{E}_\lambda\right) \tag{3.5}$$

Since $\mathrm{Tr}\,\rho = 1$ it follows that $\sum_\lambda \hat{E}_\lambda = \mathcal{I}$. If the apparatus is initially in a pure state $|\alpha\rangle$, then the measurement operators for the system alone are

$$\hat{M}_\lambda = {}_A\langle\lambda|\hat{U}(\tau)|\alpha\rangle_A. \tag{3.6}$$

This formalism stands in close analogy to Bayesian inference. There, in a classial setting, measurement is understood as an information update to the observer.

After the observation of an event λ at time $t+\tau$, the *posterior* probability $\wp_\lambda$ of an event x is given by

$$\wp_\lambda(x;t+\tau) = \frac{\wp(\lambda|x)\wp(x;t)}{\wp(\lambda)} = \frac{\wp(\lambda|x)\wp(x;t)}{\sum_y \wp(\lambda|y)\wp(y;t)}. \tag{3.7}$$

This is motivated from Bayes' rule. Being aware that a transformation of the probability distribution has taken place, we can write Equation 3.7 as

$$\wp_\lambda(t+\tau) = \frac{\mathcal{O}_\lambda \wp(t)}{\wp(\lambda)}, \tag{3.8}$$

with the coefficients of $\mathcal{O}_\lambda$ being $\mathcal{O}_\lambda(x) = E_\lambda(x) = \wp(\lambda|x)$. Clearly, the quantum case provides a generalization to this, with the probability vector $\wp$ replaced by the density operator ρ and the measurement updating (or conditioning) described by a positive operator valued measure (POVM). The last property is what allows the system to be perturbed by measurement. The conditional, posterior state does not allow full reconstruction of the prior state, before measurement.

The importance of this description for discrete, measurement-based feedback of a superconducting qubit by dispersive read-out is as follows. We recognize that in this case the measurement apparatus A is the resonator field. If the resonator mode is in a coherent state $|\alpha\rangle$, resonant with the bare resonator frequency ω_r of the resonator, the propagator $\hat{U}$ as appearing in Equation 3.1 is (in the interaction frame)

$$\hat{U}(\tau) = \exp(-i\chi\tau\sigma_z a^\dagger a).$$

This is the phase shift operator for coherent states with phase $\chi\tau\sigma_z$. Cavity decay, omitted here, simply has the effect of stabilizing the phase shift to a steady state value of $\simeq \pi/4$ (see Section 2.2), equivalent to a finite period of interaction. The qubit gets entangled with coherent pointer states [Walls and Milburn, 2008; Gambetta et al., 2008] $|\alpha_{g/e}\rangle$ of the transient field, i.e.

$$\begin{aligned}\hat{U}(|\alpha\rangle\langle\alpha|\otimes\rho)\hat{U}^\dagger = &\rho_{ee}|\alpha_e\rangle\langle\alpha_e|\otimes|e\rangle\langle e| \;+\; \rho_{eg}|\alpha_e\rangle\langle\alpha_g|\otimes|e\rangle\langle g| \;+ \\ &\rho_{ge}|\alpha_g\rangle\langle\alpha_e|\otimes|g\rangle\langle e| \;+\; \rho_{gg}|\alpha_g\rangle\langle\alpha_g|\otimes|e\rangle\langle e|.\end{aligned} \tag{3.9}$$

Measurement of the field is related to projection onto coherent states [Eichler et al., 2012a] which form an overcomplete set of Fock space. They are not orthogonal [Walls and Milburn, 2008], i.e.

$$|\langle\beta|\alpha\rangle|^2 = e^{-|\alpha-\beta|^2},$$

thus large displacements and phase shifts are necessary to best discriminate between both pointer states and achieve maximal projection of the qubit. Ideally,

the conditional states of the qubit are just its eigenstates and the measurement is QND. However, it is also clear that non-orthogonality of the pointer states causes residual uncertainty in determining the qubit state which is inherent and not due to measurement imprecision or noise.

Going back to the more abstract formalism, the link between measurement and feedback is a (classical) decision rule which for each measured data-set computes the appropriate feedback operation. Mathematically, it is an injective mapping between the set of measurement results and possible operations, $\lambda \mapsto U_\lambda$, with potentially as many different operations as there are possible outcomes. Thus the entire feedback process including measurement has the following effect on the initial density matrix ρ:

$$\rho \mapsto \mathcal{G}\rho = \sum_\lambda U_\lambda M_\lambda \rho M_\lambda^\dagger U_\lambda^\dagger = \sum_\lambda W_\lambda \rho W_\lambda^\dagger. \tag{3.10}$$

Here the feedback operation is denoted $\mathcal{G}$ and $W_\lambda = U_\lambda M_\lambda$ with measurement operators M_λ and unitary operations U_λ.

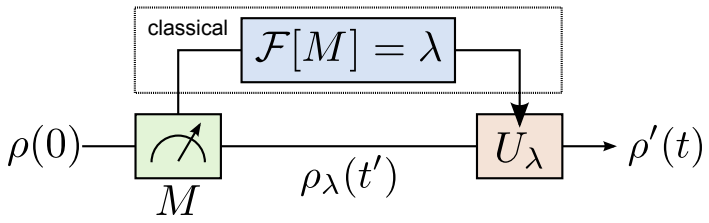

Figure 3.1: General scheme of a measurement based feedback system with measurement (green), classical information processing (blue) and conditioned feedback operation (red).

This structure, measurement followed by unitary operation, has been found to be a general property of quantum operations [Doherty et al., 2001]: From Kraus' representation theorem [Kraus, 1971] we know that the action of any quantum operation $\mathcal{O}$ (linear, completely positive and trace preserving) can be written as an expansion with bounded operators A_k:

$$\mathcal{O}\rho = \sum_k A_k \rho A_k^\dagger \tag{3.11}$$

By polar decomposition, any operator can be written as the product of a unitary and a positive operator, thus $A_k = \tilde{U}_k \tilde{M}_k$, which is analogous to the feedback operation. Doherty et al. [2001] see this as a proof that any quantum operation is achievable by means of feedback control.

3.3 Optimal filtering for qubit state estimation

In this section a brief description of filter methods for qubit state inference from a resonator transmission measurement is presented. Given a measurement record $\psi = \psi(t)$, the task is to apply a filter functional $\mathcal{F}$, linear or nonlinear, which allows for best possible discrimination between the qubit states, i.e.

$$\psi \mapsto \mathcal{F}[\psi] \mapsto \sigma_\psi. \tag{3.12}$$

The last mapping in Equation 3.12 represents a decision rule that leads to a state estimate σ_ψ, e.g. 0 or 1 for ground and excited state in the case of a two-level atom. In the simplest case it can be realized by means of a threshold θ saying that for all results with $\mathcal{F}[\psi] \geq \theta$ ($< \theta$) we opt for state 1 (0) depending on the nature of the physical process. In dispersive read-out, we can identify positive and negative answers in the right quadrature with excited and ground states, respectively, as pointed out in Section 2.2.

3.3.1 Linear filters

A linear filter functional can be represented as a convolution integral with filter kernel f over a period of length T:

$$\mathcal{F}[\psi](t) = (f * \psi)(t) = \int_{t-T}^{t} f(t-t')\psi(t')\,\mathrm{d}\,t' \tag{3.13}$$

The kernel is required to be normalized, i.e. $\int_{t-T}^{t} f(t-t')\,\mathrm{d}\,t' = 1$. Since integration extends over a compact interval we speak of a *finite impulse response* (FIR) filter. Moreover, in practice, signal processing is performed with a digitized signal on a *field programmable gate array* (FPGA) such that the convolution becomes

$$\mathcal{F}_{digital}[\psi]_k = \sum_{l=k-m+1}^{k} f_{k-l}\ \psi(t_l) \tag{3.14}$$

for a filter of length $m \geq 1$ (called m-tap filter) and discretely sampled time points t_l with separation determined by the analog-to-digital-conversion bandwidth. Gambetta et al. [2007] discussed optimal protocols for state estimation in single-shot read-out including linear and nonlinear filters. They used not the direct measurement record ψ but the integrated record up to the current observation time $s(t) = \int_0^t \psi(t')\,\mathrm{d}\,t'$. This leads to an improved signal-to-noise ratio for uncorrelated noise, because the ideal steady-state response for dispersive read-out has the form of a step function.

Possible linear filters include the box-car filter, where $f_l = 1/m \ \forall l$ or an exponential decaying filter reflecting the ensemble averaged (but not the single-shot) dynamics of qubit decay. It is understood that the form of the filter kernel f defines the type of information extracted from the measurement record which should be congruent with qubit state information. However this invokes a subtle distinction between read-out concerned with the initial qubit state and read-out that aims at extracting the current state. The latter is the relevant task in feedback. To some degree, this difference is contained in how older records are weighted relative to newer ones. For short integration times (much shorter than the relaxation time), however, the difference becomes unimportant. With knowledge of the average single-shot trace, it is possible to find an optimal filter kernel, which is specific to current measurement conditions. This has been conducted numerically by Govenius [2012], based on single-shot measurements done on the same sample as in the present work. The result was that the best estimate, conditioned on initial preparation, is obtained from filter coefficients that exhibit a three-point pattern of the form $\{f_1, f_2, f_3\} \approx \{1, -1, 1\}$. In particular the measurement fidelity does not improve significantly for filter lengths greater or equal three. Consequently, in order to minimize computational time in a real-time feedback application, a three-tap filter appears optimal. Furthermore it can be realized easily in digital signal processing since only multiplications by ± 1 are involved which are computationally cheap.

3.3.2 Bayesian filter

Next we consider nonlinear filtering. By definition Bayesian updating is the optimal procedure to infer a probability distribution from continuous monitoring Wiseman et al. [2002]; Gambetta et al. [2007]. The probability to observe the state $\rho \in \{g, e\}$ given the record ψ is

$$\wp(\rho|\psi) = \frac{\wp(\psi|\rho)\wp(\rho)}{\sum_{\rho'} \wp(\psi|\rho')\wp(\rho')}. \tag{3.15}$$

The left hand side is interpreted as a posterior probability, after the observation, while the right hand side probabilities are valid prior to the observation. On the basis of the expected evolution of an observed qubit state $\rho_{t'}$ at time t', we can compute the conditional probabilities $\wp(\psi(t)|\rho_{t'})$ to observe the quadrature amplitude $\psi(t)$ at a later time $t \geq t'$. By expected evolution it is meant that the field dynamics in the interval $[t', t]$ obeys the stochastic cavity Bloch equations (2.12) with $\sigma_z(t')$ determined by $\rho_{t'}$. With analytical solutions termed $\phi_{\rho_{t'}}(t)$, the

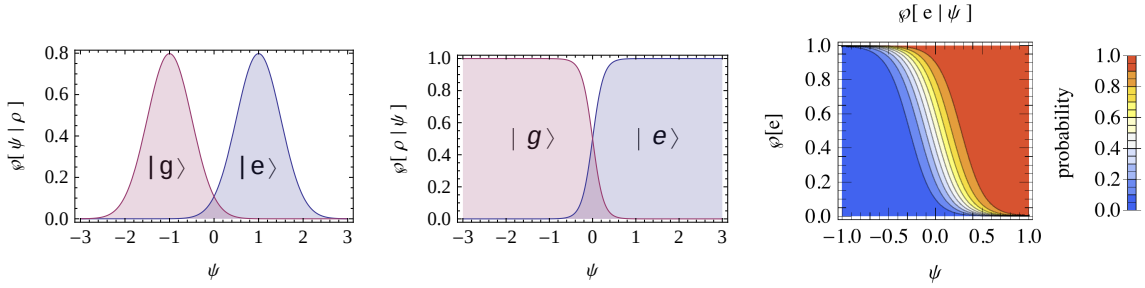

Figure 3.2: Illustration of the probability distributions involved in Bayesian filtering of a dispersive measurement record. **Left**: The density $\wp[\psi|\rho]$ for $\rho = g, e$ with a Gaussian noise distribution assumed. These are just the probability distributions for the pointer states. **Middle**: The posterior probabilities $\wp[\rho|\psi]$ according to Equation 3.15 and with $\wp[e] = \wp[g]$. **Right**: Dependence of the posterior probabilitiy $\wp[e|\psi]$ on the prior $\wp[e]$. We see that the discrimination threshold at zero gets nonlinearly biased towards the state which is more likely to have been present initially. This parameter is what varies in dynamic updating.

expression for the conditional probability is

$$\wp(\psi(t)|\rho_{t'}) = \int K\left(\frac{\psi(t) - \phi_{\rho_{t'}}(t)}{\Delta^2}\right) \mathrm{d}\,\phi_{\rho_{t'}}(t). \tag{3.16}$$

Here, a kernel function K describes the noisy signal centered around ϕ_ρ with the parameter Δ^2 being a measure of the signal fluctuations. Integration extends over all states $\phi_{\rho_{t'}}(t)$ that the measurement apparatus can reach in time $t - t'$ starting from ϕ_ρ. For example, ϕ_ρ may be the solution to the stochastic cavity Bloch equation (2.15). With exponentially distributed decay time τ_d we have

$$\begin{aligned}
\wp(\psi(t)|e_{t'}) &= \int_{t'}^{t} K\left(\frac{\psi(t) - \phi_{\tau_d}(t)}{\Delta^2}\right) \frac{e^{-\tau_d/T_1}}{T_1}\,\mathrm{d}\,\tau_d + K\left(\frac{\psi(t) - \phi_e(t)}{\Delta^2}\right) \frac{e^{-t/T_1}}{T_1}, \\
\wp(\psi(t)|g_{t'}) &= K\left(\frac{\psi(t) - \phi_g(t)}{\Delta^2}\right).
\end{aligned}$$

For example, the kernel function can be approximated by a Gaussian distribution which would be expected from coherent states. See Figure 3.2 for an illustration of the Bayesian probability distributions. It is worth noting that linear and nonlinear filters can of course be combined by modifying Equation 3.16 such that the input to K is not $\psi - \phi_\rho$ but $f * (\psi - \phi_\rho)$ for an appropriate choice of f, i.e. the nonlinear filter is applied after the linear filter: $\mathcal{F} = \mathcal{F}_{nl} \circ \mathcal{F}_{lin}$.

Alternatively, previous experimental data can be used to retrieve the probability distribution. This solution might be superior to the previous case, since it is

specifically tailored to the measurement dynamics after the signal photons leave the resonator. In the present case the most prominent contribution to nonlinearities is the paramp.

Here again, as mentioned before, it is not sufficient to measure the resonator output for an ensemble of prepared excited and ground states which yield the probability distributions $\wp(\psi(t)|g_0)$ and $\wp(\psi(t)|e_0)$. $g_{t'}/e_{t'}$ indicate ground/excited states prepared at time $t = t'$. The problem is that we really need the distributions $\wp(\psi(t)|g_t)$ and $\wp(\psi(t)|e_t)$ to reliably determine the qubit state at the present time and not that of the past. This problem can be overcome only approximately, as measurement always lags behind preparation, by conditioning not on the preparation but on the immediate past, i.e. $\wp(\psi(t)|e_{t-\delta t})$ with $\delta t \ll t$. Still, some decision rule needs to be employed to determine whether $\psi(t-\delta t)$ belongs to g or e. To set up the prior probability for Bayesian updating at this point, it might be necessary to resort to some form of linear filtering with a simple threshold decision rule. Later on, after a first posterior probability distribution has been set up, Bayesian updating works recursively. The key to implementing a Bayesian filter on an FPGA is to use the obtained (approximate) probability distribution $\wp(\psi(t)|\rho_{t-\delta t})$ as a look-up table to make an estimate for the current state $\rho(t)$. A decision rule could be obtained from evaluating

$$\psi \mapsto \mathrm{sgn}(\wp(e|\psi) - \wp(g|\psi)) = \mathrm{sgn}\left(\frac{\wp(\psi|e) - \wp(\psi|g)}{\wp(\psi|e) + \wp(\psi|g)}\right). \tag{3.17}$$

The Bayesian updating procedure is to calculate the posterior probabilities $\wp_{t+\delta t}[\rho|\psi]$ at time $t+\delta t$ from the prior probabilities $\wp_t[\rho|\psi]$ at time t, the measurement record $\wp_t[\psi]$ and the time correlations $\wp[\psi(t+\delta t) = \psi'' \wedge \psi(t) = \psi']$. In the first step, we write

$$\wp_{t+\delta t}[\rho|\psi''] = \frac{\wp[\psi(t+\delta t) = \psi''|\rho_t]\ \wp_t[\rho]}{\wp_t[\psi'']}. \tag{3.18}$$

The single terms in this equation can be expressed by the given properties via

$$\wp_t[\rho] = \sum_{\psi'} \wp_t[\rho|\psi']\ \wp_t[\psi'],$$

and

$$\begin{aligned}\wp[\psi(t+\delta t) = \psi''|\rho_t] &\equiv \sum_{\psi'} \wp[\psi(t+\delta t) = \psi''|\psi(t) = \psi']\ \ \wp_t[\psi'|\rho] \\ &= \sum_{\psi'} \wp[\psi(t+\delta t) = \psi'' \wedge \psi(t) = \psi']\ \frac{\wp_t[\rho|\psi']}{\wp_t[\rho]}.\end{aligned}$$

The final result is

$$\wp_{t+\delta t}[\rho|\psi''] = \frac{\sum_{\psi'} \wp[\psi(t+\delta t) = \psi'' \wedge \psi(t) = \psi']\ \wp_t[\rho|\psi']}{\wp_t[\psi'']}. \tag{3.19}$$

To clarify notation, we distinguish between trajectories of single measurement records $\psi : t \mapsto \psi(t)$ and the values they may assume, denoted ψ'', ψ'. The probability $\wp[\psi(t+\delta t) = \psi'' \wedge \psi(t) = \psi']$ describes the correlation that one measures ψ' at time t and ψ'' at time $t + \delta t$. In the case of $\wp[\psi(t+\delta t) = \psi''|\rho_t]$ we think of the distribution of measurement records at time $t + \delta t$ that is preceded by the state estimate ρ at time t.

From this theoretical excursion we draw an important conclusion regarding the implementation of a Bayesian filter on an FPGA. The key element is to acquire correlated histogram data of the output field after uniformly preparing the qubit in $|g\rangle$ or $|e\rangle$. Equivalently, this measurement directly yields the probability distributions $\wp_t\psi$ and $\wp[\psi(t+\delta t) = \psi'' \wedge \psi(t) = \psi']$. In order to initialize the recursion of the state estimates $\wp_t[\rho|\psi]$ one needs to resort to a threshold based method, calculate it beforehand from theory or take previously recorded data. Since the computations are rather complicated and require knowledge of the entire record, updating will need to be performed after the measurement on another computer. The next problem is limited memory which keeps the number of correlated time points low. All the same it is possible to feed the obtained probability distribution $\wp[\rho|\psi]$ from one measurement as input to the next such that two correlated histograms per measurement suffice. A more complicated task is to keep the system stable. That is all relative phases of the microwave generators need to be controlled as well as displacement and cancellation of the paramp pump and the qubit transition frequency. In turn the nonlinear filter is specifically tailored to the system dynamics. Realized as a simple look-up table, the Bayesian filter avoids multiplication that is expensive in terms of computational time and hardware. All linear filters rely on multiplication.

3.4 Summary

In this section, the notion of discrete feedback control of a quantum system was introduced. The description involves three steps: quantum measurement, classical information processing and coherent feedback operation conditioned on the measurement outcome. Quantum measurement is most generally described by a positive operator valued measure (POVM) which can be understood in terms of interaction of the system with a measurement apparatus and projection of the latter. In dispersive read-out this corresponds to indirect measurement of the qubit via detection of coherent pointer states of the transient cavity field.
Estimating the qubit state is thus achieved via linear or nonlinear filtering of the resonator output. Bayesian filtering establishes a probability distribution that is

continuously updated during the measurement record. It has been proposed (but not yet realized) that the kernel for Bayesian updating can be implemented as a look up table on an FPGA. Measuring signal correlations in single-shot read-out serves as calibration.

Chapter 4

Experimental realization of feedback

4.1 General outline of the experiment

After a general discussion of quantum feedback control in the previous section, at this point a concrete feedback application for control of a superconducting qubit is presented. Projective measurement of the qubit by strong, dispersive read-out is taken as the basis for conditioned coherent operation applied to the qubit. High fidelity single-shot read-out is realized by employing a paramp. In the experiments presented in this thesis the conditional operations are microwave Rabi pulses to the qubit with flip angles 0 and π: Depending on the measurement result, we are able to flip the qubit state or leave it as it was. It is important to note, however, that due to projection onto the measurement basis, information about the true initial state is lost. Therefore the feedback operation, neglecting qubit decay, corresponds to an essentially classical binary operation. More generally, it can be understood as an initialization procedure to prepare the qubit in either excited or ground state from an arbitrary, initially unknown state. For the same purpose that experiment has recently been conducted by Risté et al. [2012a] with a transmon qubit in a 3D cavity exhibiting relaxation times of up to 50 μs, almost 2 orders of magnitude more than what is typically achieved with the setup used for this thesis.

One motivation for this simple approach is to avoid being limited by qubit decoherence which, on the present setup, was much faster than relaxation (by a factor of 5). In fact, finite qubit relaxation and decoherence impose severe constraints on the feasibility of measurement-based feedback. There will always be a non-negligible delay between measurement and conditional operation. During that period initially extracted information is liable to get obsolete such that the feedback operation finally produces the opposite of what was intended. In the case of bit-flip, decay is in some sense the inverse operation of a π pulse from the ground to the excited state. If the qubit decays after having been identified as excited, a

π pulse will re-excite it even though it was meant to take it to the ground state.

Highly adaptive signal processing and feedback triggering have been achieved with the help of *field programmable gate array* (FPGA) electronics. Moreover, pulse generation which is usually performed by arbitrary wave form generators (AWG) of the type *Tektronix 5014* had to be revised for the feedback pulse. The reason was an inacceptably long trigger delay, i.e. the time between receiving a trigger and the output of a pulse. For the previous model the delay amounts to ~ 500 ns which could be drastically reduced to ~ 40 ns by resorting to the model *Tektronix 520*. As a further option, pulse generation on the FPGA itself was investigated.
A schematic overview of the feedback loop setup is depicted in Figure 4.1. The qubit is prepared in an arbitrary state by a pulse from the AWG Tektronix 5014. That AWG also produces the measurement pulses (green) that go through the resonator and are amplified by a Josephson parametric amplifier (JPA) and a high electron mobility transistor (HEMT). Having left the dilution refrigerator the transmitted signal passes a heterodyne down-conversion mixer and enters the FPGA (blue). There, digital signal processing electronics evaluate the feedback condition at a pre-defined delay after the start of the measurement (measure trigger). If the answer is positive, a trigger (red) is sent to the AWG Tektronix 520 which is programmed to launch a π pulse resonant with the qubit $g \leftrightarrow e$ transition. Subsequently, another measurement (green) reads out the new qubit state. A more detailed drawing is depicted in Figure 4.3 and the feedback loop inside the FPGA is explained later in Figure 4.4.

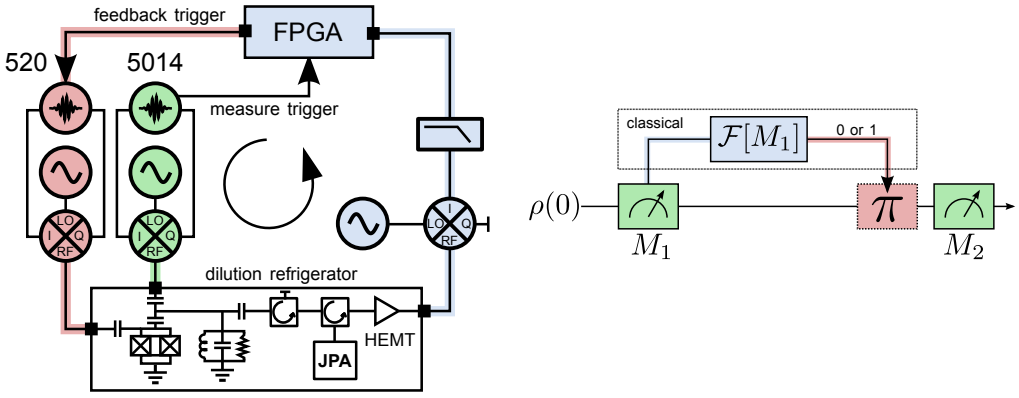

Figure 4.1: Setup (left) of the feedback experiment with the different stages highlighted in colours such that they can be identified with the abstract feedback loop (right). The stages are state preparation (green), signal processing and feedback logic (blue) and feedback operation (red).

Figure 4.2 shows the corresponding pulse sequence. Preparation and read-out pulses are operated by an AWG Tektronix 5014, the feedback π pulse is launched from an AWG Tektronix 520. For qubit control, Gaussian pulse envelopes with full width at half maximum (FWHM) $\sim$ 15 ns were employed. All pulses are up-converted to the respective transition frequencies by mixing with continuous wave microwave tones. The measurement pulse envelopes are of the type on-hold. After the observed onset of the resonator output the program waits for a preset delay Fb time until optimal read-out fidelity is reached and calculates the feedback operation. In current experiments this measurement delay amounted to 150 ns. It then takes 250 ns to launch the feedback pulse which gives 400 ns total accumulated delay after the preparation. A second measurement after the feedback pulse reads out the new qubit state.
By means of two FPGA applications we are able to extract two types of information about the feedback and measurement dynamics. Time resolved IQ histogram data cover 160 ns from first and second measurement record (blue regions). Moreover it is also possible to correlate the pre- and post-feedback quadrature data at a certain delay after the measurement onset (called Fb time). The instances when correlation is active is marked by red vertical lines.

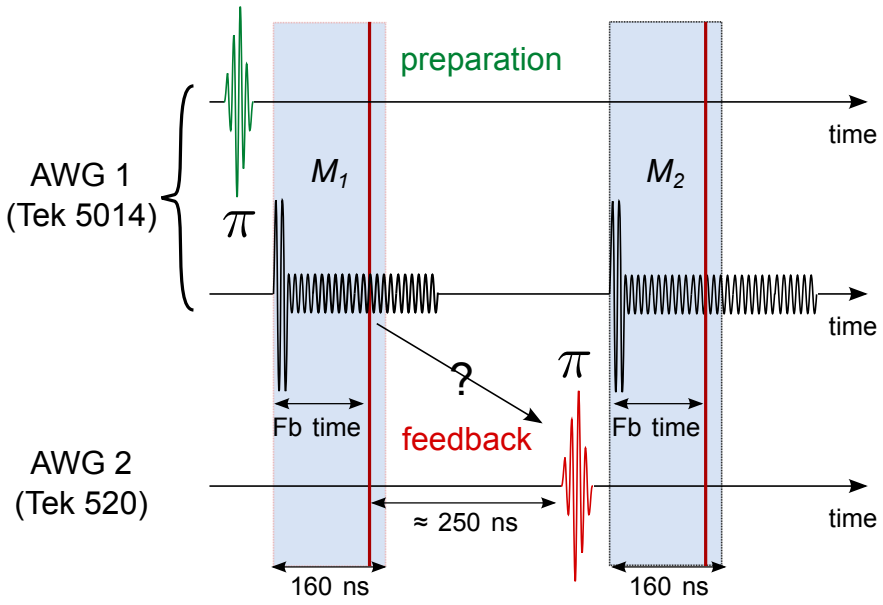

Figure 4.2: Pulse sequence used for the feedback experiment. Preparation (top) and read-out (middle) are performed by an AWG Tektronix 5014, the feedback π pulse (bottom) is launched from an AWG Tektronix 520. Blue regions indicate the time intervals covered in the time-resolved histogram mode of the feedback FPGA application. The read-out values used for the correlation type measurement are marked by red lines.

After this introduction, it is worth pointing out possible applications. Performing qubit operations conditioned on some measurement result plays a key role in quantum teleportation [Bennett et al., 1993]. There, to obtain the teleported state it is necessary to perform a qubit rotation that depends upon the result of a joint read-out of another qubit pair in the Bell basis. Instead of two there are four possible measurement results that need to be distinguished and correspondingly four different operations need to be triggered selectively. Up to the point where feedback sets in, teleportation has been successfully demonstrated in a circuit QED setup by Baur et al. [2012]. The work presented in this thesis is supposed to contribute to the implementation of a full teleportation protocol in the near future.

4.2 Experimental setup

In this chapter the experimental setup for the realization the previously introduced feedback protocol is characterized. Each feedback experiment is necessarily preceded by a series of characterization and calibration measurements which are summarized in Section A of the appendix.

Operational system parameters are noted in Table 4.2.1. All given quantities except the critical photon number $n_{crit} = \Delta^2/4g^2$ are determined from experiment. The theoretically expected dispersive shift χ (Equation 2.4) is given in brackets behind the experimental value. By means of magnetic flux the transmon $g \leftrightarrow e$ transition was tuned below the resonator frequency to enhance the relaxation time T_1 to $\simeq 970$ μs. The reasoning was that for this experiment, minimal relaxation is the decisive quantitiy for successful feedback. Still, other parameters such as the dispersive shift χ and the signal-to-noise ratio (SNR) are crucial for state identification. A maximization of the SNR as a function of critical measurement power and detuning from Equation 2.19 favored positive detunings of ~ 800 MHz. However, the observed T_1 at this spot was only $\simeq 550$ ns (compare the discussion of the SNR together with Figure 2.2).

Now, the experimental setup shown in Figure 4.3 is summarized briefly. The system consisting of a transmon qubit capacitively coupled to a coplanar waveguide resonator on-chip is placed inside a dilution refrigerator cooled down to a base temperature of 55 mK[1]. Pulses for coherent control and read out are generated

[1]Ideally 20 mK should be reached which is however a technical issue that has not been investigated further.

parameter	**value**	
ω_{ge}	6.3981	GHz
T_1	970	ns
T_2	260	ns
$g/2\pi$	67	MHz
$E_C/\hbar$	344	MHz
$\omega_{r,g}$	7.1334	GHz
$\kappa/2\pi$	6.4505	MHz
$\chi/2\pi$	-1.7 (-1.9)	MHz
n_{crit}	31	

Table 4.2.1: Overview of the most important parameters of the qubit-resonator system.

by AWGs *Tektronix 5014* and *520* and get shifted to frequency bands centered at the corresponding transition frequencies by mixing with local oscillator microwave tones. These are provided by microwave generators *Agilent 8648A*.
The mixers, of type *Marki 4509IQ*. are all operated at the left side-band at an intermediate frequency (IF) of 100 MHz, meaning that pulse envelopes are modulated with a 100 MHz oscillation. This way any direct current (dc) signal leakage through the mixer is detuned from the actual resonance frequency by 100 MHz and unwanted excitation is avoided. Mixer calibration encompasses dc offset calibration, performed for both AWGs, and sideband calibration which is performed only for the *Tektronix 5014*. The latter optimizes the phase and amplitude of the IF modulation such that the sideband chosen for operation has maximal amplitude and the others are minimal. Since the AWG *Tektronix 520* is not configured for generating appropriate pattern sequence files for sideband calibration that procedure was omitted. Since no interference at the other sideband was to be expected this did not pose a problem for our work. Due to lack of voltage output/input ports, dc offset calibration for the *Tektronix 520* has been established externally via bias-tees *ZFBT - 4R2GW*. Mixer sideband calibration for the *Tektronix 520* has not been solved within this work.
Measurement of the resonator output field is accomplished by heterodyne down coversion with an LO microwave tone detuned by 25 MHz from the resonator transition frequency. An IF of 25 MHz has been chosen for reasons of frequency matching with the FPGA analog to digital conversion (ADC) bandwidth of 100 MHz. Down conversion is succeeded by an analog low pass filter before the signal enters the FPGA.

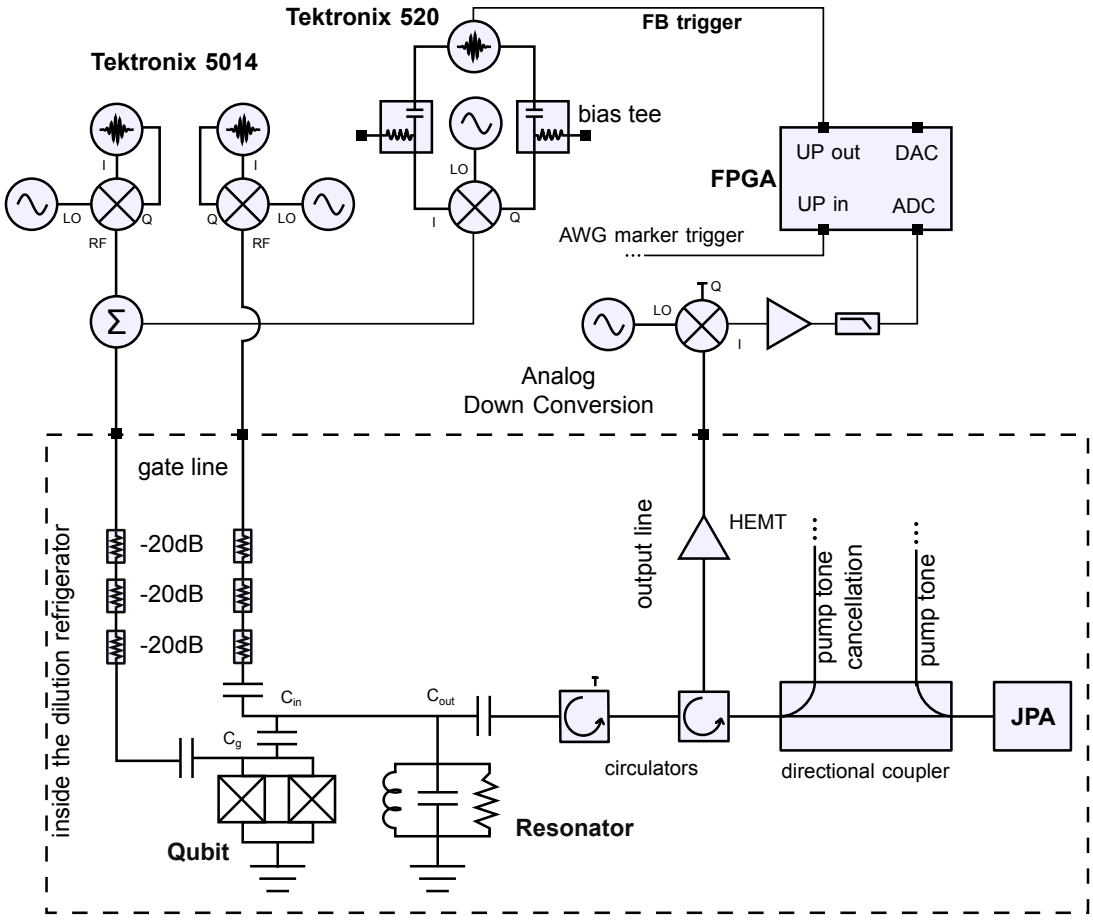

Figure 4.3: Detailed view of the experimental setup including the inside of the dilution refrigerator, as an extension to Figure 4.1.

4.3 FPGA programming

4.3.1 General facts and digital signal processing

Signal processing in science faces huge challenges posed by large amounts of data, varying information content and high bandwidth measurements. In feedback type experiments, high bandwidth data processing is vital to ensure real-time communication with the system. Field programmable gate arrays (FPGA) account for that flexibility. They are digital integrated circuits which allow for parallel computing and can get re-programmed easily such that different applications are executable from the same hardware.

Parallel computing is achieved by a *pipelined* operational structure: In contrast to standard CPUs processing units on the FPGA can take new inputs even if processing of previous inputs has not yet finished. As in a pipeline, data flow is continuous with time synchronization provided by an external clock.
Moreover, the FPGA can be reprogrammed rapidly in order to switch between different tasks. The elementary building blocks are look-up tables (LUT) that represent arbitrary logical/binary operations and programmable switch matrices (PSM) which interconnect the LUTs. In order to change the functionality of the FPGA signal paths can be re-routed by means of the PSMs and LUTs can be assigned different truth tables. In addition to the LUTs there exist specialized building blocks, e.g. FIR filters for signal processing, and a block random access memory (RAM).
FPGA programs are written in the "Very High Speed Integrated Circuit Hardware Description Language" (VHDL). In practice, the applications are generated by means of the software *Simulink* by MathWorks Inc. and are subsequently compiled into VHDL with the package *ISE Design Suite* provided by Xilinx Inc. The graphical representation of the block wiring in Simulink allows FPGA programming even without explicit knowledge of VHDL.

The FPGA used for this work was a *Virtex 4* by Xilinx Inc. [Xilinx Inc., 2008] contained in the *Nallatech DSP Xtreme Development Kit IV* [Nallatech Limited, 2005]. Digital to analog conversion (DAC) of incoming signal is achieved at a sampling frequency of 100 MHz with 14 bit resolution. There are two input channels that handle a maximal range of ± 1.1 V each. Included in the DAC are anti-alias and low-pass filters as well as a dc block. Triggers enter and leave via four so-called user_pins that are mapped to boolean signals by means of a threshold. Moreover, digital to analog (DAC) output can be produced. For feedback applicability it is relevant to know the delays between signal input and trigger/pulse output without processing in between. These have been measured to be 70 ns for ADC to user_pin and 250 ns for ADC to DAC. The latter is significantly higher due to filters and buffers needed to convert from analog to digital and back. These delays

are certainly not optimal as they are a non-negligible on the time scale of qubit relaxation and decoherence. In addition there are delays due to signal propagation, analog filtering and triggering the feedback pulse. The technical realization of an ideal feedback apparatus, favorably in analog manner, that accomplishes both measurement and feedback operation would be an objective for future work. In this thesis, however, the primary interest was to show feasibility and gain some experience with the experimental setup.

In digital signal processing as performed on the FPGA, data is represented in binary format. In general, the binary representation is realized by processing each signal bit on another channel. Associating several channels allows to construct arbitrary rational numbers in a given range (There are only finitely many channels). We distinguish between two data types: *boolean* and *fixed point*. Boolean signifies truth values where 0 and 1 are identified with "False" and "True", respectively, which requires only one channel. The binary representation of an integer,

$$(b_{n-1}, \ldots, b_0)_2 \equiv \sum_{k=0}^{n-1} b_k 2^k \tag{4.1}$$

is constructed from concatenating n channels each carrying the signal b_k. b_{n-1} is called the most significant bit (MSB) and b_0 the least significant bit (LSB). It is now possible to introduce a *sign-bit* and a *binary point* that allows to define negative numbers and fractions. The sign-bit is the MSB of the string and indicates positivity (negativity) if it is 0 (1). A binary point of $0 \leq m \leq n$ merely indicates that the representation of Equation 4.1 is multiplied by 2^{-m}. Signed fixed points are denoted FIX_n_m where n is the bit width (length of the string) including sign-bit and m is the position of the binary point; unsigned fixed points are called UFIX_n_m.

There are various operations that manipulate binary strings. We can take away a certain *bit range* of the string, e.g. $bit_{[k:l]}[(b_{n-1}, \ldots, b_0)_2] := (b_k, \ldots, b_l)_2$, or *reinterpret* it in another format, e.g. unsigned instead of signed or with binary point set to 0, or *cast* it to another format, e.g. increase or decrease the string length. Moreover there are elementary arithmetic manipulations such as addition and multiplication.

All these operations need to be implemented in hardware by connecting signal paths in a specific manner. In order to ensure stable signal processing, certain operations may need to get clocked if path delays get too long. This is achieved by including *delays* into the path that suspend the signal until the next external clock signal. Moreover computationally complex blocks, such as multiplication have built-in delays. One of the objectives in realizing the feedback loop was minimizing these delays such that measurement information remains valid.

For boolean manipulations there are logical blocks such as and ($\wedge$), or ($\vee$), inv ($\neg$), etc. More sophisticated elements are *multiplexers*, *addressable shift registers*

and *registers*. Registers can store binary data by providing an input, enable and reset port. Multiplexers allow to choose from a tuple of inputs by taking as further argument the index of the input selected for transmission. Addressable shift registers are a sort of combination of registers and a multiplexer. Incoming data shifts "through" the registers by one position each clock cycle. Via an address input port the register is determined that creates the output. Feeding a constant value to the address input port simply leads to a delay of variable length. Further useful blocks include *counters* and *accumulators* which perform the tasks they are called after.

4.3.2 Implementation of the feedback loop

At this point the FPGA firmware that controls the feedback loop is discussed. A block diagram description is shown in Figure 4.4. There, the path belonging to the feedback loop is highlighted in green, the blocks belonging to the DDC are yellow, the feedback evaluation logic is painted blue and the data acquisition is depicted in red. At the input port to the left we have the user_pins for triggers and the analog-to-digital conversion (ADC) port for the signal. The signal is first mixed with a LO at 25 MHz for heterodyne detection of both quadratures. Next comes a FIR filter including scaling and subtraction of a constant value. Data address tuples for histogram binning on a RAM are formed in the box labelled address. The feedback trigger is formed by evaluating the feedback condition $I(t_{fb}) \geq (<)\theta$ with the parameters Fb time t_{fb}, Fb threshold θ and Fb polarity $\geq$ ($<$) read from a register. Note that the threshold is actually subtracted beforehand but kept here for better understanding. The triggers A/B are used to adjust the correct feedback delay with an addressable shift register (ASR). By inverting the boolean function 2^{nd}Measurement we assure that the feedback trigger is given only during the first measurement. All triggers and logic outputs (blue) are boolean variables. INV stands for *invert* and exchanges the booleans 0 (`false`) and 1 (`true`). The feedback trigger leaves the FPGA via user_pin 3 towards the AWG Tektronix 520. Optionally pulse generation may take place in the FPGA already such that a pulse is output on the output channels of the digital-to-analog conversion (DAC) port.

Before entering the FPGA, the signal passes first an analog down-conversion with LO frequency detuned from the measurement frequency by an IF of 25 MHz. This matches the sampling rate of the FPGA, 100 MHz, in that precisely four processing steps can be performed within a period of the IF oscillation. A subsequent band-pass filter protects the FPGA from dc and counteracts aliasing due to digital sampling. After the analog-to-digital conversion (ADC) of the FPGA the first signal processing unit is the *digital-down-conversion (DDC) block*. There, heterodyne detection of the incoming signal is performed. To this end the signal

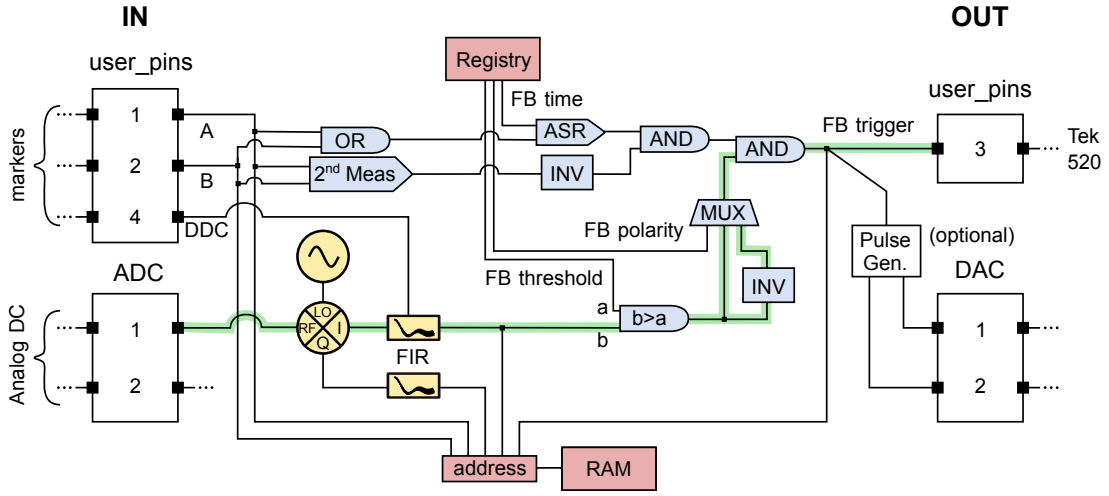

Figure 4.4: Diagrammatic description of the FPGA feedback application. The signal-to-feedback path is highlighted in green, the DDC blocks are yellow, the feedback evaluation logic is shown blue and the data acquisition is depicted in red

is split up and multiplied by a sine or cosine with the IF frequency 25 MHz, respectively, to form I and Q quadratures. This is easily and rapidly achieved by multiplication with the periodic sequence $\{1, 0, -1, 0\}$, each such block covering 40 ns which explains the choice of a 25 MHz IF. Another phase-adjustable mixing option is available, too, but would consume too much time in the feedback loop due to multiplication.

Since mixing creates both difference and sum frequencies a *finite-impulse-response (FIR) filter* follows the DDC which necessarily has to have nodes at 25 and 50 MHz. As in the feedback loop our main concern is speed, the simplest way of doing this is a four-tap, i.e. 40 ns, square window filter which has the typical sinc form in the frequency domain. On the FPGA that filter is implemented by means of an addressable shift register which variably delays the incoming signal point and subtracts it from a free running accumulation of all previous signal points. Hence, only the values within the time window are kept and the signal processing in real-time is achieved. An alternative to this fast yet crude method is a 40-tap FIR filter with programmable filter coefficients. Again, multiplication of binary data and the sheer filter length are too time consuming to be applicable for feedback within the bounds given by the qubit relaxation time. The extra delay is of the order of 1 μs. In fact filter length is a problem only if the latest signal entry (carrying new information) is given less significance, by the value of its filter coefficient, than is given to older entries. As already discussed, filters used in real-time processing for feedback need to be sensitive to the information content and should not include avoidable delay. Different options built-in in series

include a three-tap version of the curvature-sensitive filter and signal integration. The total delay amounts to 10 ns at minimum for the slender version, each of the last options takes one more delay of 10 ns.

Before the down-converted and filtered data is processed further, a pre-processing unit allows to subtract offsets and subsequently scale the data. The aim of this unit is to efficiently use all memory available for data storage. In the histogrammer application the entire IQ phase space record is stored with a resolution between five and seven bits, depending on the type of application. In the course of digital signal processing data resolution is reduced stepwise from the initial 14 bit output of the ADC. If the data range is too low chopping away too many digits behind the binary point will irreversibly lead to a bad resolution. The combination of subtraction and scaling thus allows to retain the best possible resolution. Furthermore it is important to note that the value subtracted from the I quadrature already defines the threshold to distinguish between ground and excited state traces in dispersive measurement.

At this point the paths leading to "feedback loop" and "signal maths" split up. In *signal maths* the quadrature representation (I, Q) can be converted to amplitude-phase (A, φ) representation. In the FPGA two signal channels entering the ADC are processed in parallel. In the signal maths block they can be multiplied to calculate correlation functions. The problem of limited resolution also renders (A, φ) histograms invaluable to retrieve accurate phase information, e.g. for calibration, because cartesian and polar representation are linked via a nonlinear transformation.

Evaluating the feedback condition requires three questions to be answered which are encoded in the parameters Fb time, Fb polarity and Subl1/2 (see Table 4.3.1). Fb time defines the read-out time t_{fb} in the first measurement at which the feedback condition is evaluated. It is the delay after the first recorded data point in the first measurement. In total 16 data points are recorded in each of the two measurements (one after preparation, one after feedback). The threshold θ defined to distinguish ground state response from excited state response can be adjusted via subtraction, i.e. it is contained in the parameter Subl. At the same time all histograms get centered around the threshold. Finally, we want to choose the target state, i.e. whether the feedback π pulse is given conditioned on ground or excited state. This is contained in Fb polarity, which can be either $\geq$ or $<$ and correspondingly defines the feedback condition as $I(t_{fb}) \geq \theta$ or $I(t_{fb}) < \theta$.

Timing in the feedback loop entirely depends on external triggers that enter

the FPGA via the *user-pins*. There are three types of triggers, A, B and DDC, referring to inputs from three different userpins. The fourth userpin serves as an output port for the feedback trigger addressing the AWG *Tektronix 520*. The trigger DDC is merely for reset of certain functions in the DDC block, such as the phase of the digital LO signal. Triggers A and B are for separate use only and have the purpose to mark different experimental settings. For example, trigger A may indicate that the qubit was initially prepared in the ground state, while trigger B signifies excited state preparation. Both triggers are handled equivalently throughout the entire application, their significance lies in establishing statistics about state preparation. Since triggers are programmed in the pulse sequence on the marker channels, this two channel option enables one to concatenate two sequences with alternating ground and excited state preparation and account for long term fluctuations. Whether trigger A or B was active is stored in the so-called diff-Bit.

The feedback application was designed for a two-step experiment with two measurement periods. Each measurement requires the FPGA to be triggered in advance, by how much needs to be determined experimentally. As a matter of consistency, each trigger has to be given twice in a row. In order to keep track of the measurement time, the rising edge of each incoming trigger is prolonged to 160 ns. This long trigger is linked to the enable port of a counter going up from 0 to 15 in the first, and from 16 to 31 in the second measurement. Reset of the counter happens after the second trigger has arrived: A register gives the boolean `true` after the falling edge of the first trigger, say A. To achieve reset after the second trigger, the register output is joined with the falling edge of A by a logical `and` and fed back to the reset port of the register. This gives a boolean `Is Second Measurement?` which is not only used to reset the counter for measurement time, but also to allow feedback triggers only during the first measurement (by inverting it). An *enable*-trigger for the feedback evaluation is realized by joining the inverted `Is Second Measurement?` with the trigger rising edge of trigger `A or B` by an `and`. This one still needs to be delayed by Fb time to form the Fb enable. The feedback trigger may then arise from the `and` combination of the Fb enable and the sign-bit of the I quadrature voltage.

4.3.3 Histogrammer and tv-mode application

Next to feedback triggering, the FPGA also stores the measured quadrature data after signal processing. In principle there are two ways to do this. Either the time traces recorded for different pulse sequences are stored as a whole, as is the case in the feedback *tv-mode* application. Labelling the pulse sequences generated by

parameter	values	significance	belongs to
Filter type	"filter library", "boxcar 4-pt", "none"	choose FIR filter for the DDC	fir_filter
post-filtering	"none", "binary filter"	enable curvature sensitive filter	fir_filter
integration	"no", "yes"	enable integration	fir_filter
Scale I1/2	2^n (n=0,1,...,6)	scale factor for $I_{1/2}$ quadrature	signalMath_v02
Scale Q1/2	2^n (n=0,1,...,6)	scale factor for $Q_{1/2}$ quadrature	signalMath_v02
SubI1/2	$[-1, 1]$	subtract value from $I_{1/2}$ quadrature (28 bit resolution)	signalMath_v02
SubQ1/2	$[-1, 1]$	subtract value from $Q_{1/2}$ quadrature (28 bit resolution)	signalMath_v02
representation	IQ, $A\varphi$	save histograms in IQ or $A\varphi$ representation	signalMath_v02
Fb polarity	$\geq$, $<$	Fb is given if the I voltage is ≥ 0, < 0, respectively	feedback_v04
Fb time	0,1,...,15	time for evaluation of the Fb condition in first measurement	feedback_v04
pointEXP	$\mathbb{N}$	number of averages	hist2D_v02
Hist3DTimeResV03	–	choose between "time-resolved" or "correlator" option	hist2D_v02

Table 4.3.1: This table gives an overview of the options for operating the histogrammer operation. They can be adjusted in the control panels of the *Labview*-application *Cleansweep* indicated in the right column.

the AWG with an index k, this corresponds to the mapping

$$(k, t) \mapsto s_k(t) = I_k(t) + iQ_k(t). \tag{4.2}$$

t denotes time in the measurement which is actually a discrete variable. Averaging corresponds to adding up time traces that belong to the same pulse sequence. Thus all statistical information except the arithmetic mean is discarded. For the feedback application, however, it would be of interest to have a rough indicator of the signal-to-noise ratio, too, such as the variance. Storing the average square of the signal would allow to extract the variance since for any random variable X, $Var[X] = E[(X - E[X])^2] = E[X^2] - E[X]^2$, with E denoting the expectation value.

In order to tackle both hindrances mentioned before, a histogram application has been designed that is capable of storing single-shot data in form of *time-resolved* (TR) quadrature histograms covering two measurement periods of 160 ns each. Such time-resolved histograms have the only disadvantage, that all information about time correlations is lost: In the feedback experiment, e.g., we cannot identify data points in the first measurement of a particular single-shot trace with those in the second measurement. To account for that problem, the application provides an option that allows to switch to another mode of operation called *correlator* (CORR). There, quadrature data is stored only at the feedback time and for first and second measurement together.

Both options can be understood best by looking at the structure of the histogram output, meaning the indexing of the histogram bins (summarized in Table 4.3.2). First, we look at the TR histogrammer. The available information is composed of the initial qubit preparation ("diff-bit") db, the "feedback-bit" fb, the measurement time t and the quadrature values I and Q. All of these variables are represented by binary strings of various length (see Table 4.3.2) that are concatenated to form a binary address string of 21 bits. For the TR histogrammer, the ordering is

$$(lsb(t), db, fb, I, Q, bit_{>0}(t)). \tag{4.3}$$

There is a technical reason for splitting off the LSB of t ($lsb(t)$) from the rest ($bit_{>0}(t)$) and putting it to the MSB position of the address string: Recording data at 100MHz is challenging, and indeed this is only possible because there are two RAM banks. By convention, the MSB of the address decides upon which of the two RAM banks to write on. The LSB of t alternates uniformly between 0 and 1 reflecting the alternation of even and odd numbers. Thus, even times t are written on RAM bank A and odd times on RAM bank B. Later, when retrieving the measurement record this has to be undone. In fact, the address is a binary

number, so Equation 4.3 actually means (according to Table 4.3.2) that

$$address = lsb(t) \cdot 2^{20} + db \cdot 2^{19} + fb \cdot 2^{18} + I \cdot 2^{11} + Q \cdot 2^4 + bit_{>0}(t)).$$

Similarly, the correlator features the variables initial qubit preparation (diff-bit) db, the quadrature values I_1 and Q_1 at the delay Fb time in the first measurement pulse and the quadrature data I_2 and Q_2 at the same delay in the second measurement pulse. The ordering in the address is now

$$(db, I_1, Q_1, I_2, Q_2).$$

Note that the address being a (binary) number implies that data is stored in vectorial form. To obtain an array with components corresponding to the variables that make up the address, the indices need to be decoded according to the structure above. That, as well as functions to generate marginal distributions of the histogram data, has been realized in a *Mathematica* script.

parameter	**binary format**	**used in mode**
diff-bit	boolean	TR, CORR
fb-bit	boolean	TR
time t	UFIX_5_0	TR
I , Q	FIX_7_6	TR
$I_{1,2}$, $Q_{1,2}$	FIX_5_4	CORR

Table 4.3.2: Summary of the address parameters used in the two histogram applications. The address strings have 21 bit resolution in total

4.4 Summary

In this chapter a description of the feedback experiment conducted in this thesis has been given. The procedure is to dispersively measure a single transmon qubit via a capacitively coupled coplanar waveguide resonator, digitally process the measurement record on an FPGA and apply a π pulse conditioned on either ground or excited state response. These latter cases are called negative and positive feedback, respectively.
The current setup has been designed in order to minimize the feedback delay down to 250 ns including main contributions from ADC, digital signal processing and triggering the feedback pulse on an AWG Tektronix 520.
Independent of the feedback loop, the FPGA also stores the obtained single shot data in form of histograms. There are several histogram options to choose from: Heterodyne data is either recorded in a time resolved or a correlated manner, linking the pre- with the post-feedback state. Moreover, next to the standard quadrature (I,Q) representation we may switch to the polar (A,φ) representation which is directly calculated. The advantage of histogram data over single traces is its compact form which allows to rapidly analyze experimental data.

Chapter 5

Analysis of experimental results

In this chapter experimental results constituting a proof-of-principle of the novel FPGA feedback apparatus are analyzed and discussed. The techniques rely entirely on the newly developed *histogram* and synchronized *tv-mode* FPGA applications for feedback. In fact, all measurements are preceded by calibration of the qubit-resonator-paramp system as described in Section A.

5.1 Histogram single-shot data

We conducted experiments with a feedback loop as depicted in Figures 4.2 and 4.1. For single-shot analysis with the histogram application, ground and excited initial states of the qubit were prepared alternatingly. For each histogram, a total of 65'536 single-shot traces for each prepared state were accumulated. Moreover, for each setting of the feedback loop (including filters, data representation, etc.) we recorded data from three different protocols. First came a reference measurement with the microwave generator for feedback switched off, such that feedback was disabled. Thereafter it was turned on again and the effect of Rabi π pulses conditioned on excited states was measured. This corresponds to a FB polarity of 0 ($\geq$) and will be called *positive feedback* in the following. Likewise we repeated the experiment with the π pulse applied to ground states (FB polarity = 1, $<$), denoted *negative feedback*. The terminology is to be understood in terms of qubit relaxation. Positive feedback aims at preparing a ground state and should thus accelerate relaxation. In contrast, negative feedback prepares excited states and thus counteracts relaxation.

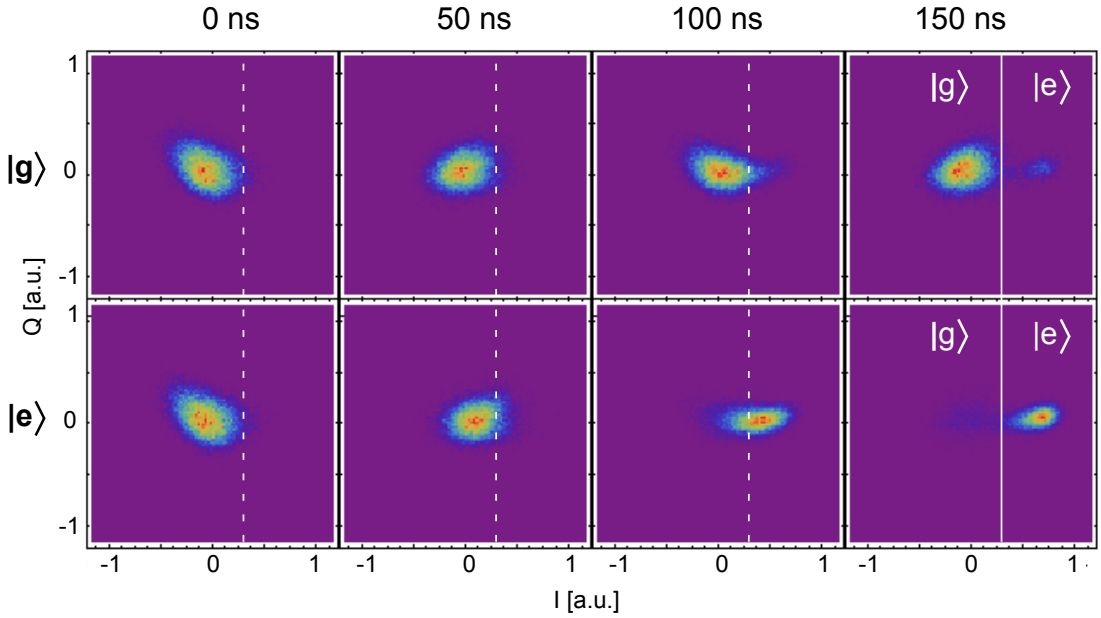

Figure 5.1: Time evolution of the transmitted resonator field during the first 150 ns of the measured output. The upper row shows the response for the qubit prepared in the ground state, the bottom row has the qubit prepared in the excited state. Initially, there is no state information (0 ns) while full separation of the qubit states is achieved at 150 ns.

5.1.1 Measurement dynamics and fidelity

Time resolved histogram data primarily gives insight into the dynamics of dispersive read-out. This is plotted in terms of the full IQ phase space record in Figure 5.1 and in form of marginal distributions of the in-phase quadrature I, that contains all qubit state information, in Figure 5.3. It is observed how ground and excited state responses initially overlap completely and gradually get more discernible in the course of the measurement process. Hence, qubit projection onto $|g\rangle$ or $|e\rangle$ gets more and more effective with longer read-out.

In order to quantify state discrimination we used the threshold method from Section 3.3 and computed the measurement fidelity $F = 1 - \Pr[e|g] - \Pr[g|e]$. It is related to the probability that no detection error has occurred. Of course, the fidelity depends on the parameters discrimination threshold and read-out time which is plotted in Figure 5.2. Since data is stored in forms of histograms that are discrete approximations to the probability density $f_{\rho_0}(i, q, t)$, these conditional probabilities are easily calculated via

$$\Pr{}_{\theta}[g_t|\rho_0] = \int_{-a}^{a}\int_{-a}^{\theta} f_{\rho_0}(i, q, t)\,\mathrm{d}\,i\,\mathrm{d}\,q.$$

for initial state ρ_0, threshold θ and the IQ data range $[-a, a] \times [-a, a]$ covered

by the histogram. For the feedback experiment, we choose the values of discrimination threshold and integration time such that the read-out fidelity is maximal. This procedure is motivated from the fact that successful feedback requires reliable state information.

From the fidelity plot 5.2 we learn that the maximum fidelity was 0.80 at an integration time of 150 ns after the measurement onset. Unfortunately there is no more data beyond this point such that we do not know for sure if this is the true maximum before saturation due to T_1 relaxation sets in. An upper bound to the fidelity, ignoring random excitation, is given by $1 - e^{-\Delta t/T_1} \simeq 0.86$, meaning that the fidelity reached in experiment is close to being T_1 limited. All the same, an integration time of 150 ns is presumably to be not the best of what can be achieved. The resonator rise time is limited by the cavity decay time $1/\kappa \simeq 26.5$ ns and analog filtering dominated by the paramp bandwidth on the order of 10 MHz (or 100 ns). The rate of information acquisition could still be improved by varying the measurement pulse shape and optimizing the read-out power. However, phase matching between paramp pump, resonator drive and down-conversion LO also has an important influence on the SNR. Telling from the qudrature plots in Figure 5.1 it is probably at this point where SNR can potentially be improved most.

There are several observations that can be extracted from this data set. First, in Figures 5.1 (IQ) and 5.3 we notice that $|g\rangle$ and $|e\rangle$ responses have quite different distributions in phase space and show different dynamics. First, noise in the $|g\rangle$ response is much larger. Moreover, unlike what is theoretically expected in a

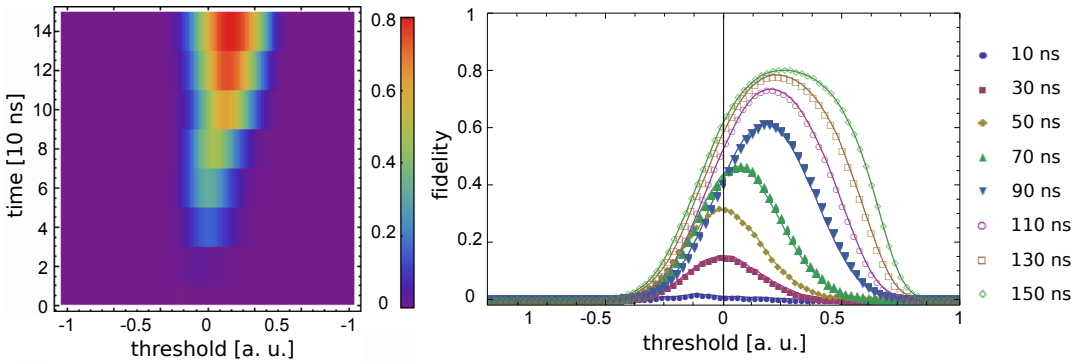

Figure 5.2: Here, the measurement fidelity is plotted as a function of measurement time and threshold (left panel). Additionally, individual points in time are selected to better visualize the threshold dependence (right panel). This is used to determine the optimal timing and threshold in feedback experiments. Lines are guides to the eye.

phase-sensitive measurement, the application of the measurement tone does not induce any shift of the $|g\rangle$ response. Only the $|e\rangle$ response is shifted and slightly squeezed. Possible reasons for this behaviour include the calibration of the paramp gain curve and the measurement frequency. From the gain curve in Figure A.5 it can be concluded that the amplified bandwidth is quite large and the gain is not uniform in the region around the pump frequency. This implies that noise with frequency components irrelevant to the read-out might get amplified. Additionally it is likely that the read-out frequency was detuned from the bare resonator frequency ω_r with a tendency towards the ground state frequency $\omega_r - \chi$. This causes a transfer of information from the phase to the amplitude, or from the I to the Q quadrature. The latter is not observable because Q is attenuated due to the phase-sensitive paramp. Additionally this might explain why there is as much noise in the $|g\rangle$ response. If the pump frequency is degenerate with $\omega_r - \chi = \omega_{r,g}$ then pump leakage will add to the $|g\rangle$ response and contribute to its noise level.

Moreover from the histograms in Figures 5.3 and 5.1 it is observable, that there is non-negligible steady-state excitation of the qubit. This is not result of the relatively high base temperature of $\simeq$ 55 mK in the cryostat which theoretically amounts to only 0.3% thermal excitation. Instead it might be possible that this excitation is due to an average photon number of $\langle n \rangle \simeq 4$ during the measurement, about 10% of the critical limit. Other sources of spurious excitation are possible but were not investigated within this work.

Finally we remark that the threshold chosen in experiment was not optimal. The FPGA application sets the origin of the I quadrature to the manually input threshold which is determined from a calibration measurement. It is more likely that the incorrect threshold in the present data was caused by a computational error than by any interim perturbation of the system. The phase between all

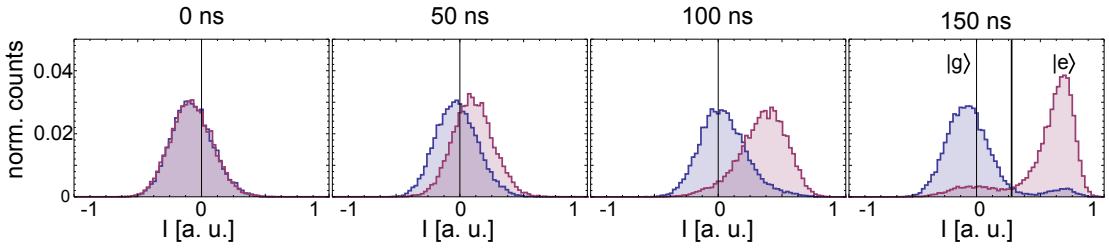

Figure 5.3: Time evolution of the I quadrature only, as compared to Figure 5.1. The distributions for initally prepared ground and excited states are shown in blue and red, respectively. Note that the $|g\rangle$ response is quasi stationary.

three measurements (reference, pos. and neg. feedback) is quite stable. All the same, near the optimal integration time the fidelity curve broadens such that small variations of the threshold around the maximum do not lead to big errors. From Figure 5.2 can be read that the experimentally achieved fidelity was only about 60% instead of the optimal 80%.

5.1.2 The effect of feedback

In this section the effect of feedback is analyzed, based on the results of the second measurement and by comparison with the reference records. Next to time-resolved data that are deprived of correlations between pre- and post-feedback state, we have also explicitly probed these correlations. This gives deeper insight into the paths of population transfer and the changes induced by feedback. Feedback errors are directly observed, too.

Positive feedback has the objective of bringing the qubit to the ground state while negative feedback aims at stabilizing an excited state. Indeed, Figures 5.4 and 5.5 not only show that the final read-out after feedback accumulates at the respective target state, but also gives the same answer for each prepared input state. This reflects that information about the input state is lost. However, it is

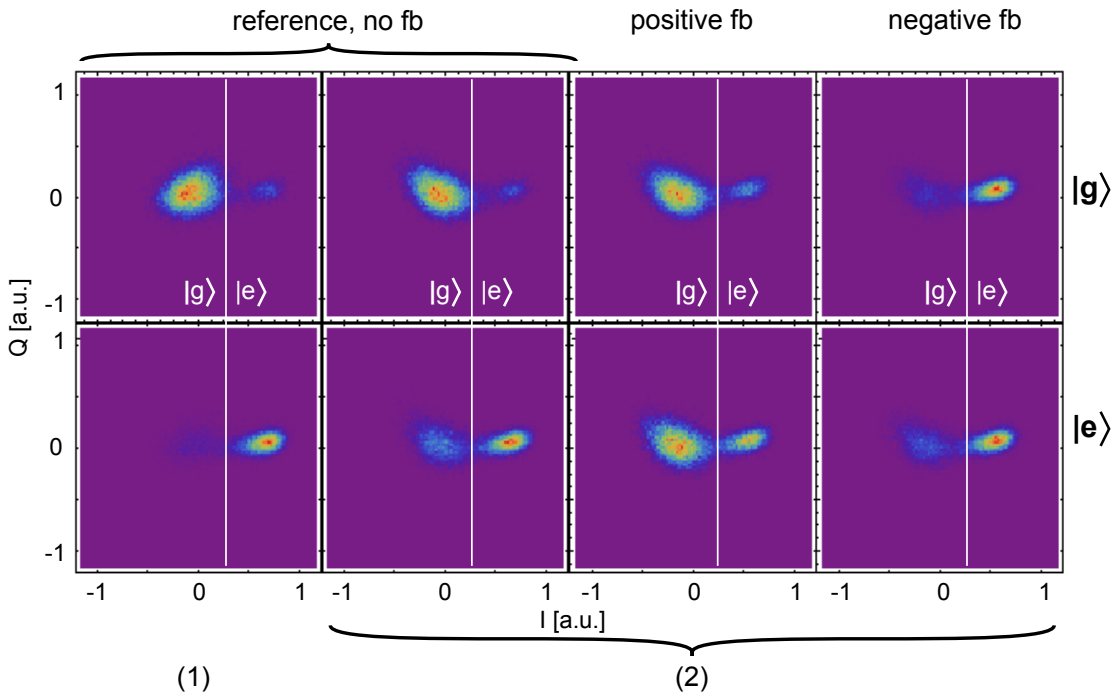

Figure 5.4: This figure shows the effect of feedback in both field quadratures. Again, the top row shows initially prepared ground states and the bottom row excited states. All phase space histograms were recorded at a delay of 150 ns after the preceding pulse (preparation or feedback) which was also the read-out time for feedback. The first two columns are reference measurements (after preparation and feedback) with feedback deactivated. In the columns to the right the records for positive and negative feedback in the second measurement are depicted. (1) and (2) refer to first and second measurement, respectively.

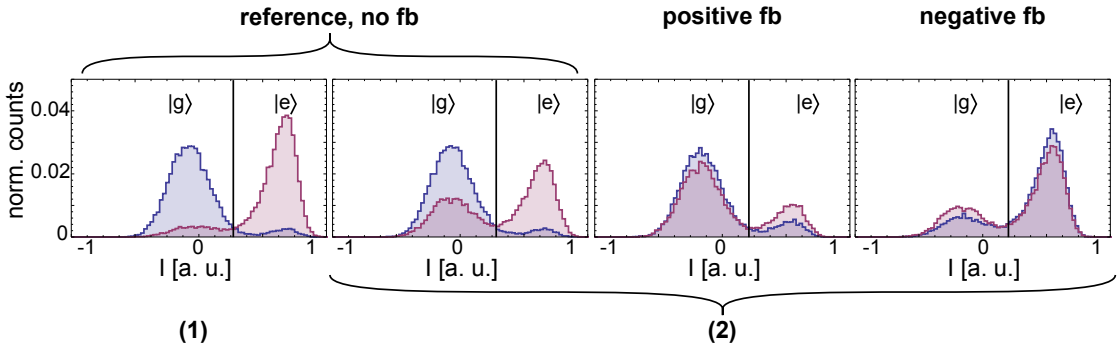

Figure 5.5: This plot shows the same data as in Figure 5.4 but only the marginal distribution over the I quadrature which renders state information a lot more visible. The threshold for feedback was set at zero in the experiment. Apparently, the optimal threshold is shifted slightly towards positive values.

also observed that the quadrature distributions do not so much concentrate on the target state but rather spread out over both, ground and excited state response. Due to errors in the protocol there is hence an increase in entropy.
Investigating the error sources we find two major contributions. One is that misidentified states lead to the opposite of the desired result. A threshold shifted from the optimal position produces a bias such that one of the two states is determined better at the expense of the other. Consequently the feedback errors in reaching the thus "handicapped" state are higher than for the other. In the present data the threshold is biased towards the ground state response and thus positive feedback is flawed. This effect becomes most evident in the correlated histograms (Figure 5.6).
More importantly, relaxation from the excited state into the ground state during measurement and feedback operation is significant since $\Delta t/T_1 \simeq 0.25$. This corrupts negative feedback in the obvious way and positive feedback in that correctly identified $|e\rangle$ states decay in between measurement and feedback. Thus they get re-excited by the feedback π pulse. Additionally the final state estimate is delayed by another 150 ns reducing the fidelity to bring the qubit to the excited state. Of course there is also the initial measurement delay that involves relaxation. For feedback, however, we only care about the qubit state information at the instance of the feedback decision. Clearly, due to the limited measurement bandwidth one cannot speak of a distinct point in time but nonetheless we account for qubit decay after preparation.

Correlating the records before, I_1, and after feedback, I_2, reveals the paths of population transfer (see Figure 5.6). Any such histogram can be subdivided into four regions corresponding to the correlations $e \to e$, $e \to g$, $g \to g$ and $g \to e$.

If thermal excitation in the steady state is low, then only the first three occur in a system without feedback, apparent in the reference measurements. Without feedback (left column in Figure 5.6), emphasis lies on the autocorrelation terms $e \to e$ and $g \to g$. Relaxation in between the measurements ($e \to g$) is with 37% contribution (see Table 5.1.1) a non-negligible contribution.
With feedback active this picture changes profoundly. Ideally, positive feedback should leave the $g \to g$ path untouched but flip $e \to e$ with $e \to g$. That it flips the latter is easily understood by noting that $e \to g$ describes decays after measuring $|e\rangle$. Thus the feedback π-pulse will re-excite in these cases. In an analogous manner, negative feedback fixes $e \to e$ but interchanges $g \to g$ with $g \to e$. In summary, positive and negative feedback put weight to the $e \to g$ and $g \to e$ correlations, respectively.
So far we only described feedback with relaxation, but without detection errors due to a bad threshold. A closer look at the region between experimental (solid line) and optimal (dashed line) discrimination threshold, $[\theta_{exp}, \theta_{opt}]$ on the I_1 axis, reveals this effect. There, the population transfer is directed opposite to the correct feedback action. Moreover, confinement to the region $[\theta_{exp}, \theta_{opt}]$ is lost in the second measurement, i.e. the I_2 axis, which indicates uncorrelated noise.

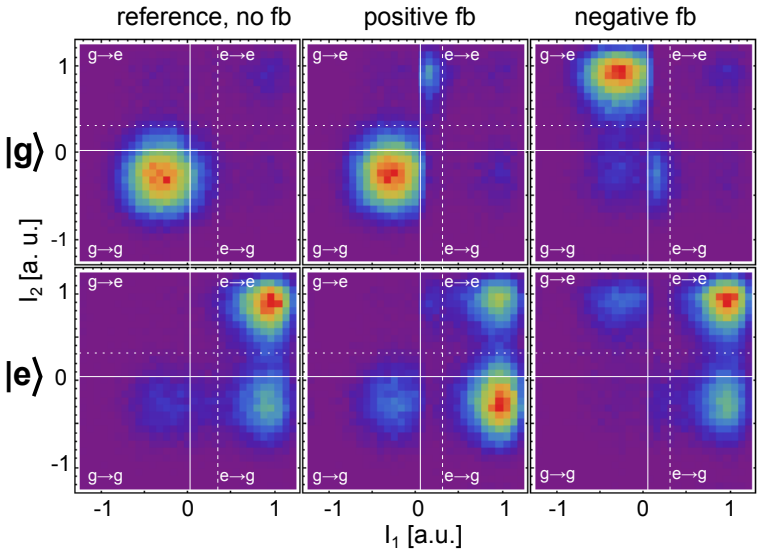

Figure 5.6: Correlations between first and second measurement record for reference measurement without feedback (left), positive feedback (middle) and negative feedback (right). The solid and dashed white lines indicate the experimental and the optimal threshold, respectively. Each plot is subdivided into the regions of discrete population transfer correlations $\rho_1 \to \rho_2$ ($\rho_{1,2} \in \{g, e\}$). These regions are bounded by the optimal threshold.

As a general result, feedback errors, due relaxation or mis-identification, lead to a population transfer that is opposite to the one desired. Due to their probabilistic nature, the two errors cannot cancel on average. We note that it might be desirable to detect the ground state more reliably since it is most stable.

Next we look at the conditional probabilities listed in Table 5.1.1. There are four types of binary parameters: qubit preparation ρ_0, first measurement record ρ_1, second measurement record ρ_2 and the feedback response σ_{fb}. The first measurement record (ρ_1) is conditioned on preparation (ρ_0) and the second measurement record (ρ_2) is conditioned on preparation (ρ_0), feedback response σ_{fb} and first measurement record (ρ_1). To calculate the state probabilities from measurement the optimal threshold was used. Instead, σ_{fb} obviously refers to the experimental threshold which makes it interesting to compare σ_{fb} and ρ_1. The probabilities $\Pr[\rho_2|\rho_1]$ are obtained from correlated data, all others are based on time resolved measurements. $\sigma_{fb} = 1(0)$ signifies that the feedback operation was triggered (not triggered).

The probabilities $\Pr[\rho_1|\rho_0]$ are merely a restatement of the read-out quality and concern the measurement fidelity only. Feedback effects can be read from the remaining probabilities, only. In general we learn that the probability to reach any target state (ρ_2), provided the initial (ρ_0) or initially measured state (ρ_1) was the ground state, is always superior to that obtained from starting in the excited state. Moreover, this discrepancy is even stronger for conditioning on the initially measured state which is actually relevant for feedback. Another important fact is that positive feedback and negative feedback produce significant errors in stabilizing states, i.e. for $\rho_2 = \rho_1$, by comparison with the reference. Thus feedback is actually harmful in these particular situations. Another interesting aspect is revealed by comparison of $\Pr[\rho_2|\rho_1]$ with $\Pr[\rho_2|\sigma_{fb}]$. For example in negative feedback, we see that if a π-pulse was triggered ($\sigma_{fb} = 1$), the subsequent excited state

probability	**no FB**	**pos. FB ($\geq$)**	**neg. FB ($<$)**
$\Pr[\rho_1 = e\|\rho_0 = g]$	0.07	0.07	0.08
$\Pr[\rho_1 = e\|\rho_0 = e]$	0.86	0.79	0.81
$\Pr[\rho_2 = e\|\rho_0 = g]$	0.07	0.14	0.77
$\Pr[\rho_2 = e\|\rho_0 = e]$	0.58	0.27	0.67
$\Pr[\rho_2 = e\|\sigma_{fb} = 0]$	0.04	0.04	0.58
$\Pr[\rho_2 = e\|\sigma_{fb} = 1]$	0.51	0.37	0.86
$\Pr[\rho_2 = e\|\rho_1 = g]$	0.05	0.11	0.79
$\Pr[\rho_2 = e\|\rho_1 = e]$	0.63	0.32	0.61

Table 5.1.1: Conditional probabilities for all three feedback scenarios.

probability is very high (0.86) while it is rather low (0.58) if it was not triggered ($\sigma_{fb} = 0$). The reverse is true for positive feedback. Together, this is a clear hint that qubit states were not properly discriminated (threshold error), i.e. a significant number of ground states was identified as excited states.

The correlated histograms (Figure 5.6) also visualize a discrepancy for measured excitation $\Pr[\rho_1 = e|\rho_0 = e]$ between reference and feedback experiments. This is also manifest in the much larger population of the $g \to g$ correlation for reference and positive fb. In feedback experiments there remains $\simeq 6\%$ less excitation at the integration time (see Table 5.1.1). The only experimental difference between these data sets lies in the microwave generator for the feedback pulse being turned off during the reference measurement. We conclude that leakage from this microwave generator seems to deteriorate the quality of the preparation pulses or inflict state mixing upon the qubit. The latter possibility is actually ruled out since the effect appears only for preparation of the excited state and does not lead to increased excitation of initial ground states.

When looking at the conditioned time evolution of identified ground and excited states after feedback in Figure 5.7, we remark that the best results are obtained if the identified state was a ground state which corresponds to fb=0(1) for positive (negative) feedback. This is plausible because the ground state is stable and the threshold is such that there is little uncertainty in the estimate.

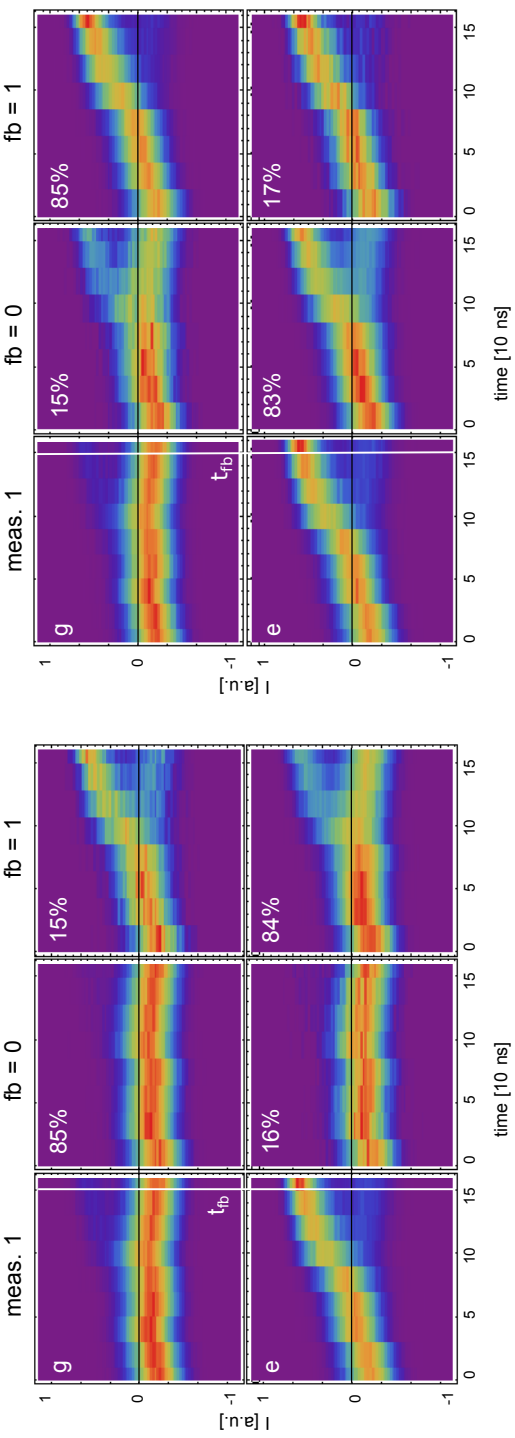

Figure 5.7: These figures show the conditioned time evolution of identified ground and excited states of the qubit after feedback. Prepared ground states are shown in the top row, excited states in the bottom row, the black horizontal line indicates the threshold. The cases of positive and negative feedback are shown in the panels to the left and right, respectively. Column one depicts the measurement before feedback. At $t = t_{fb}$ all traces below the threshold are identified with ground states and all those above the threshold with excited states. The following two columns show traces for which feedback was given (fb = 1) or not (fb = 0). Inside each panel, the probability ($\Pr[\sigma_{fb}|\rho_0]$) with which the particular case occurred is indicated.

5.1.3 Evaluation of the feedback efficiency

Finally it is interesting to assess the quality of the feedback protocol. To this end we define the feedback efficiency as the probability to reach the target state $|\psi\rangle$ which is related to the state fidelity

$$\eta_\psi = \mathrm{Tr}\left(\rho|\psi\rangle\langle\psi|\right) = \langle\psi|\rho|\psi\rangle.$$

For positive and negative feedback the target states are $|g\rangle$ and $|e\rangle$, respectively. In total, the final qubit excited state population was 0.72 for negative and 0.20 for positive feedback. The feedback efficiencies were thus 0.72 and 0.80 respectively. Without feedback, the remaining excitation amounts to 0.33. These values are averaged over all preparations in both, ground and excited state which is equivalent to an inital totally mixed state $(|e\rangle\langle e| + |g\rangle\langle g|)/2$.
These values confirm that negative feedback, although more difficult due to the instablility of the excited state, has performed quite well and positive feedback could do better. Certainly, more careful calibration of the threshold and the paramp would contribute much to improve the efficiency. Still, the ultimate limitation will always be due to T_1 relaxation beacuse the feedback delay leads to $\simeq 22\%$ decay between measurement and feedback operation.
Note that instead of pure target states, one could obtain more general target states that account for relaxation from a calculation according to the feedback Kraus representation in Equation 3.10 with modified Kraus operators ($\lambda = e, g$)

$$W_\lambda = U_\lambda \, e^{\mathcal{L}t_f} \, M_\lambda(t_m). \tag{5.1}$$

This accounts for the feedback delay t_f and the measurement operators include the time t_m needed to generate the state estimate. Free open system evolution is given by the Liouvillian $\mathcal{L}$ ($\dot{\rho} = \mathcal{L}\rho$). A simplified version would be to replace $M_\lambda(t_m)$ by $\Pi_\lambda e^{\mathcal{L}t_m}$ with projectors Π_λ onto the qubit σ_z eigenstates.

In order to characterize the feedback process in greater detail it is advantageous to study the doubly conditional probabilites given in Table 5.1.2. Han-

probability	**no FB**	**pos. FB ($\geq$)**	**neg. FB ($<$)**
$\Pr[\rho_2 = e \vert \rho_0 = g \wedge \sigma_{fb} = 0]$	0.04 (0.35)	0.04 (0.42)	0.29 (0.08)
$\Pr[\rho_2 = e \vert \rho_0 = g \wedge \sigma_{fb} = 1]$	0.16 (0.15)	0.65 (0.08)	0.86 (0.42)
$\Pr[\rho_2 = e \vert \rho_0 = e \wedge \sigma_{fb} = 0]$	0.04 (0.04)	0.04 (0.08)	0.63 (0.42)
$\Pr[\rho_2 = e \vert \rho_0 = e \wedge \sigma_{fb} = 1]$	0.62 (0.46)	0.31 (0.42)	0.86 (0.08)

Table 5.1.2: Double conditional probabilities for all three cases. Second measurement record (ρ_2) conditioned on preparation (ρ_0) and feedback (σ_{fb}). The values in brackets give the probabilities $\Pr[\sigma_{fb} \wedge \rho_0]$ with which the condition events occur.

dling conditional probabilities without knowing the corresponding base rates, i.e. the probabilities with which the condition events occurred, is sometimes misleading. Thus these are also written down as a reference. For example the values $\Pr[\rho_2 = e|\rho_0 = g \wedge \sigma_{fb} = 1] = 0.65$ for positive feedback and $\Pr[\rho_2 = e|\rho_0 = g \wedge \sigma_{fb} = 0] = 0.29$ for negative feedback seem astonishingly high. However, the events $\{\rho_0 = g \wedge \sigma_{fb} = 1, 0\}$ occurred only with probability 0.08 in the respective feedback modes, a reason why errors can affect them more strongly. On the other hand we have in mind that next to spurious excitation, these are mostly the cases where true $|g\rangle$ states have been misidentified as $|e\rangle$ due to the biased threshold. We remark that for the qubit initially prepared in $|e\rangle$ these errors are smaller which speaks for $|e\rangle$ states being identified reliably if they have not decayed.

Finally we note that in an ideal scenario the events $\{\rho_0 = g, e \wedge \sigma_{fb} = 0\}$ should be equivalent. This is simply a restatement of the fact that feedback depends only on the measurement outcome used for deciding upon whether to apply a π pulse or not. As seen from the table, this holds true only for $\Pr[\rho_2 = e|\rho_0 = g, e \wedge \sigma_{fb} = 1]$ in negative feedback and $\Pr[\rho_2 = e|\rho_0 = g, e \wedge \sigma_{fb} = 0]$ in positive feedback. For the rest, the discrepancies might again arise from state misidentification on the basis of a biased threshold.

5.2 Suppression of Rabi oscillations

Up to this point, considering ground and excited states only, an essentially classical description of the feedback operation was sufficient. Now it is of further interest to interpolate between these two poles of the Bloch sphere and consider arbitrary superpositions. This was realized by replacing the initial zero or π pulse for state preparation with Rabi pulses of flip angle ϑ. In the Bloch sphere representation, these pure states are

$$|\vartheta, \varphi\rangle = \cos(\vartheta/2)\, e^{-i\varphi/2}|g\rangle + \sin(\vartheta/2)\, e^{i\varphi/2}|e\rangle. \tag{5.2}$$

Here, φ is a phase angle which corresponds to the rotation axis (0 for x and π for the y-axis). Ideally, the first measurement projects the superposition state onto the z-axis of the Bloch sphere and destroys quantum coherence. With probabilities $\cos^2(\vartheta/2)$ and $\sin^2(\vartheta/2)$ we find the qubit in the ground and excited state, respectively. If we assume the measurement to be QND and neglect decay, then the qubit will remain in the state onto which it has been projected until the feedback pulse arrives. The result of the feedback should be the same as for preparation of ground or excited state. However, decay is not negligible as we have seen in the previous sections. Thus with increasing Rabi angle feedback fidelity will deteriorate.

Rabi measurements produce ensemble averaged time traces. Usually the qubit population is inferred by a fit to the cavity Bloch equations [Bianchetti et al., 2009] introduced in Section 2.2:

$$\Pr[\rho = |e\rangle\langle e|] = \frac{1}{T}\int_0^T \left(\frac{s_\rho(t) - \hat{s}_g(t)}{\hat{s}_e(t) - \hat{s}_g(t)}\right) \mathrm{d}\, t. \tag{5.3}$$

Where the hat ˆ indicates theoretical traces which are solutions to the cavity Bloch equations and s is a single quadrature signal (I or Q). Integration always extends over the full measurement record.
However phase-sensitive parametric amplification destroys information in the attenuated quadrature. Moreover the first measurement is much shorter than qubit relaxation time. Both make it hard to apply cavity Bloch fits for determining the qubit population. Thus a modification to Equation 5.3 could be made by replacing the theoretical ground and excited state response with the observed responses for hypothetical ground and excited states. Moreover, due to divergences, a further change to Equation 5.3 was made to obtain the relative excitations

$$\Pr{}'[\rho = |e\rangle\langle e|] = \frac{\int_0^T (s_\rho(t) - \hat{s}_g(t))\, \mathrm{d}\, t}{\int_0^T (\hat{s}_e(t) - \hat{s}_g(t))\, \mathrm{d}\, t}. \tag{5.4}$$

The reference traces $\hat{s}_{g,e}$ were determined experimentally: Excited state traces were produced with (calibrated) π pulses directly before the measurement pulse and measuring without any pulse yielded the ground state traces. For the first measurement these were the Rabi traces with corresponding Rabi angles. For the second measurement we switched off the microwave generator for qubit preparation and set the threshold such that the feedback π-pulse was triggered always or never.

As it turned out, switching feedback microwave generator on and off slightly influenced the Rabi dynamics. An increase in the Rabi frequency by $\simeq 17\%$ and a decrease in the Rabi amplitude of up to $\simeq 15\%$ was observed when the microwave generator was on (see Figure 5.8 on the left). This implies off-resonant driving which possibly originate residual leakage of the LO signal through the up-conversion mixer. By populating the resonator the qubit transition can get a.c. Stark shifted. Direct driving of the qubit is unlikely due to the detuning of the microwave source by an IF of 100 MHz.
From a technical perspective, mixer calibration for that microwave generator was delicate, because the AWG Tektronix 520 does not possess d.c. input ports for both of its channels. D.c. offset calibration was therefore realized by means of bias tees controlled by another AWG Tektronix 5014.
All the same this feature lead to the difficulty that signal and reference traces had to have the same microwave generator activity (on/off). Otherwise negative populations were obtained. For that reason we normalized each Rabi record by

subtracting the ground state response from the same record and dividing by the largest achieved difference $\int_0^T (\hat{s}_e - \hat{s}_g)\,\mathrm{d}\,t$ for that particular measurement period (1 or 2). For the first measurement this was the "no feedback" trace, for the second the difference between negative and positive feedback traces for ground state preparation was largest. By this method only relative excitations are extracted such that the amplitude modulations are comparable but not the absolute values of excitation.

Finally, the suppression effect on Rabi oscillation by means of a conditioned π pulse is displayed in the middle of Figure 5.8. It is apparent that this works quite well for ground states and gradually declines with increasing Rabi angle until the excited state. The same effect has been observed in the previous data, even though not as strong, and was related to threshold bias and relaxation. Here these effects occur, too. In particular, determining the optimal threshold is hard as the average traces do not contain any information about the real statistics. Actually the threshold can be adopted directly from histogram single-shot data since both application are fully synchronized. However both experiments need different FPGA triggers such that new pulse patterns need to be loaded onto the AWGs. Unfortunately this reprogramming also destroys phase relations such that these have to be recalibrated entirely and the thresholds may not coincide any longer.

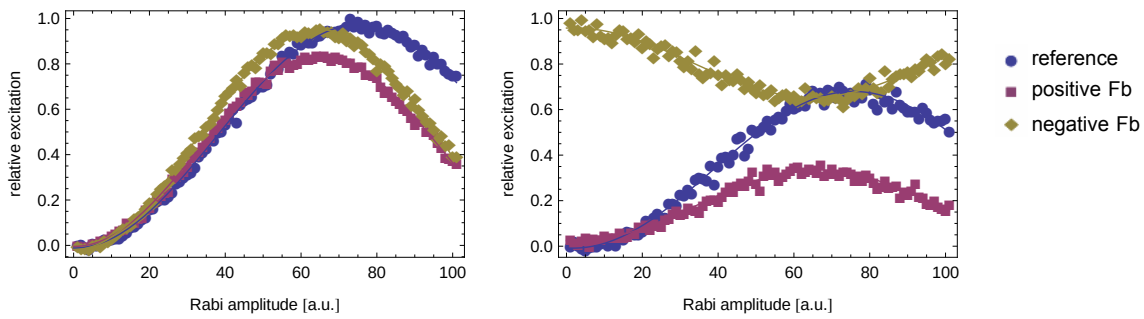

Figure 5.8: Partial suppression of Rabi oscillations due to feedback. Only relative excitations are plotted as absolute populations could not be reliably determined. **Left:** Rabi oscillations obtained in the first measurement. There is an increase in the Rabi frequency and a decrease in the excitation amplitude when the microwave generator for feedback is turned on; in the reference measurement it is switched off. **Right:** Rabi oscillations are partially suppressed and inverted as an effect of a conditioned π pulse on $|e\rangle$ and $|g\rangle$, respectively.

5.3 Summary

The discrete feedback protocol to deterministically steer a transmon qubit towards ground or excited state, called positive and negative feedback, respectively, has been tested successfully. The achieved probabilities to reach either state were 0.80 and 0.72 for ground and excited state which compares to 0.67 and 0.33 without feedback.

Some sources of errors have been recognized by analysis of time resolved single shot histograms and correlations between the pre- and post-feedback states. The main issues were the QND nature of the measurement, signal to noise ratio, the discrimination threshold and qubit decay in between state identification and feedback operation.
As an effect of the enhanced measurement power corresponding to 4 photons on average random excitations of the qubit amounting to $\simeq 7\%$ for prepared ground states were observed. This is to be taken as a hint that the measurement was not entirely QND and hence contributes slightly to a distortion of the feedback operation. On the other hand, in order to make the pointer states distinguishable SNR needs to be sufficiently high. The reason for the failure of 1 photon measurements to achieve full separation is deemed to lie in a detuning from the bare resonator frequency that distributes qubit information over both quadratures. This reduces the effectiveness of phase sensitive amplification. Additionally, noise from pump leakage might have excessively broadened the ground state response which is supposed to have been degenerate in frequency with the pump.
We found that the experimentally adjusted threshold did not coincide with the theoretically optimal threshold. Thus state mis-identification made the feedback produce the opposite result of what was intended. These were clearly visible in the correlated histograms which also gave detailed insight in the paths of population transfer from the first measurement to the second.
Finally, qubit decay was the most important source for errors. The pure feedback delay amounts to 250 ns which is about one quarter of the qubit relaxation time. This is accompanied by 150 ns integration time to determined the qubit state with maximal SNR. Apparently this substantially contributed to feedback being less efficient if the initially measured (or prepared) state was an excited state.
Recently, similar experiments have been conducted by Risté et al. [2012a]. The main difference to this work lay in the experimental setup with a 3D cavity enabling a qubit relaxation time of up to 50 μs. Accordingly, state discrimination was almost perfect with fidelities after initialization by measurement [Risté et al., 2012b] above 90%. On the contrary digital signal processing was not performed on an FPGA and thus took more than 4 μs which is about 20 times longer than what was achieved in this work.

Chapter 6

Conclusion

This thesis applies several concepts of circuit QED and quantum optics for the experimental implementation of a discrete feedback protocol to deterministically prepare ground and excited states in a superconducting transmon qubit. A quantum non-demolition measurement of the qubit state is followed by classical information processing to compute the appropriate feedback operation, i.e. a π pulse. With the help of field-programmable gate array electronics a feedback response time of 250 ns was realized which is well below the measured relaxation time (T_1) of 970 ns. Thus the application developed here demonstrates a first step towards real-time signal processing in a circuit QED architecture. Despite non-negligible errors, the experimentally achieved target state fidelities after feedback amounted to 80% for the ground state and 72 % for the excited state. These were obtained with uniform intitial preparation in either of the two states.

The most important limitations to the protocol were identified to be the feedback delay between measurement and feedback operation, and single shot read out fidelity. Both need to be improved in order to make the scheme more reliable and allow generalisations for applications in quantum error correction or teleportation. This goes along with taking the step towards multi-qubit read-out as well as active calibration of the read-out apparatus. Since phase sensitive amplification is involved the relative phases of three microwave tones need to be matched and possibly re-adapted throughout the experiment.

Feedback delay, i.e. the time it takes to compute and trigger the feedback operation, may not be decreased by much if digital signal processing is involved. Some improvements are to be expected from an FPGA with a bandwidth in the GHz range (such as *Xilinx Virtex 6*) but probably analog devices need to be employed for that particular task. Moreover, the detour of triggering pulses on an AWG might be avoidable if a continuous qubit drive is directly modulated by the output

of the feedback device.

Still, the question arises how qubit state estimation can be designed efficiently in an analog and continuous scenario. In fact, recent applications of Bayesian updating either use linearizations [Vijay et al., 2012] or operate at optical frequencies with feedback iteration times on the order of 100 μs [Sayrin et al., 2011]. The latter is about three orders of magnitude larger than what is required for superconducting circuits. On the other hand, working with three dimensional cavities instead of coplanar waveguide resonators can enhance qubit coherence times by about one to two orders of magnitude [Paik et al., 2011]. For such a setup, our FPGA based feedback protocol would already be fast enough to address more complex tasks.

Bibliography

C. Ahn, A. C. Doherty, and A. J. Landahl. Continuous quantum error correction via quantum feedback control. *Phys. Rev. A*, 65:042301, Mar 2002. doi: 10.1103/PhysRevA.65.042301.

M. A. Armen, J. K. Au, J. K. Stockton, A. C. Doherty, and H. Mabuchi. Adaptive homodyne measurement of optical phase. *Phys. Rev. Lett.*, 89:133602, Sep 2002. doi: 10.1103/PhysRevLett.89.133602.

M. Baur, A. Fedorov, L. Steffen, S. Filipp, M. P. da Silva, and A. Wallraff. Benchmarking a quantum teleportation protocol in superconducting circuits using tomography and an entanglement witness. *Phys. Rev. Lett.*, 108:040502, Jan 2012. doi: 10.1103/PhysRevLett.108.040502.

C. H. Bennett, G. Brassard, C. Crépeau, R. Jozsa, A. Peres, and W. K. Wootters. Teleporting an unknown quantum state via dual classical and einstein-podolsky-rosen channels. *Phys. Rev. Lett.*, 70:1895–1899, Mar 1993. doi: 10.1103/PhysRevLett.70.1895.

N. Bergeal, F. Schackert, M. Metcalfe, R. Vijay, V. E. Manucharyan, L. Frunzio, D. E. Prober, R. J. Schoelkopf, S. M. Girvin, and M. H. Devoret. Phase-preserving amplification near the quantum limit with a josephson ring modulator. *Nature*, 465(7294):64–68, May 2010. ISSN 0028-0836.

R. Bianchetti, S. Filipp, M. Baur, J. M. Fink, M. Göppl, P. J. Leek, L. Steffen, A. Blais, and A. Wallraff. Dynamics of dispersive single-qubit readout in circuit quantum electrodynamics. *Phys. Rev. A*, 80:043840, Oct 2009. doi: 10.1103/PhysRevA.80.043840.

A. Blais, R.-S. Huang, A. Wallraff, S. M. Girvin, and R. J. Schoelkopf. Cavity quantum electrodynamics for superconducting electrical circuits: An architecture for quantum computation. *Phys. Rev. A*, 69:062320, Jun 2004. doi: 10.1103/PhysRevA.69.062320.

A. Blais, J. Gambetta, A. Wallraff, D. I. Schuster, S. M. Girvin, M. H. Devoret, and R. J. Schoelkopf. Quantum-information processing with circuit quantum

electrodynamics. *Phys. Rev. A*, 75:032329, Mar 2007. doi: 10.1103/PhysRevA.75.032329.

M. Boissonneault, J. M. Gambetta, and A. Blais. Dispersive regime of circuit qed: Photon-dependent qubit dephasing and relaxation rates. *Phys. Rev. A*, 79: 013819, Jan 2009. doi: 10.1103/PhysRevA.79.013819.

L. Bouten, R. van Handel, and M. James. An introduction to quantum filtering. *SIAM J. Control Optim.*, 46,:2199–2241,2007, 2007.

C. M. Caves. Quantum limits on noise in linear amplifiers. *Phys. Rev. D*, 26: 1817–1839, Oct 1982. doi: 10.1103/PhysRevD.26.1817.

J. I. Cirac and P. Zoller. Quantum computations with cold trapped ions. *Phys. Rev. Lett.*, 74:4091–4094, May 1995. doi: 10.1103/PhysRevLett.74.4091.

A. A. Clerk, M. H. Devoret, S. M. Girvin, F. Marquardt, and R. J. Schoelkopf. Introduction to quantum noise, measurement, and amplification. *Rev. Mod. Phys.*, 82:1155–1208, Apr 2010. doi: 10.1103/RevModPhys.82.1155.

C. Cohen-Tannoudji, J. Dupont-Roc, and G. Grynberg. *Atom - Photon Interactions: Basic Processes and Applications*. John Wiley and Sons, Inc., 1998.

M. H. Devoret, A. Wallraff, and J. M. Martinis. Superconducting qubits: A short review. *arXiv:cond-mat/0411174*, 2007.

A. C. Doherty, S. Habib, K. Jacobs, H. Mabuchi, and S. M. Tan. Quantum feedback control and classical control theory. *Phys. Rev. A*, 62:012105, Jun 2000. doi: 10.1103/PhysRevA.62.012105.

A. C. Doherty, K. Jacobs, and G. Jungman. Information, disturbance, and hamiltonian quantum feedback control. *Phys. Rev. A*, 63:062306, May 2001. doi: 10.1103/PhysRevA.63.062306.

C. Eichler, D. Bozyigit, and A. Wallraff. Characterizing quantum microwave radiation and its entanglement with superconducting qubits using linear detectors. *Phys. Rev. A*, 86,:032106, June 2012a.

C. Eichler, C. Lang, J. M. Fink, J. Govenius, S. Filipp, and A. Wallraff. Observation of entanglement between itinerant microwave photons and a superconducting qubit. *arXiv:1209.0441*, Sept. 2012b.

A. Fedorov, L. Steffen, M. Baur, M. P. da Silva, and A. Wallraff. Implementation of a toffoli gate with superconducting circuits. *Nature*, 481(7380):170–172, jan 2012. ISSN 0028-0836. doi: 10.1038/nature10713.

J. Gambetta, A. Blais, D. I. Schuster, A. Wallraff, L. Frunzio, J. Majer, M. H. Devoret, S. M. Girvin, and R. J. Schoelkopf. Qubit-photon interactions in a cavity: Measurement-induced dephasing and number splitting. *Phys. Rev. A*, 74:042318, Oct 2006. doi: 10.1103/PhysRevA.74.042318.

J. Gambetta, W. A. Braff, A. Wallraff, S. M. Girvin, and R. J. Schoelkopf. Protocols for optimal readout of qubits using a continuous quantum nondemolition measurement. *Phys. Rev. A*, 76:012325, Jul 2007. doi: 10.1103/PhysRevA.76.012325.

J. Gambetta, A. Blais, M. Boissonneault, A. A. Houck, D. I. Schuster, and S. M. Girvin. Quantum trajectory approach to circuit qed: Quantum jumps and the zeno effect. *Phys. Rev. A*, 77:012112, Jan 2008. doi: 10.1103/PhysRevA.77.012112.

C. W. Gardiner and M. J. Collett. Input and output in damped quantum systems: Quantum stochastic differential equations and the master equation. *Phys. Rev. A*, 31:3761–3774, Jun 1985. doi: 10.1103/PhysRevA.31.3761.

J. Govenius. Single-shot qubit readout in circuit qed using parametric amplification. Master's thesis, ETH Zürich, 2012.

J. Koch, T. M. Yu, J. Gambetta, A. A. Houck, D. I. Schuster, J. Majer, A. Blais, M. H. Devoret, S. M. Girvin, and R. J. Schoelkopf. Charge-insensitive qubit design derived from the cooper pair box. *Phys. Rev. A*, 76:042319, Oct 2007. doi: 10.1103/PhysRevA.76.042319.

K. Kraus. General state changes in quantum theory. *Annals of Physics*, 64(2):311 – 335, 1971. ISSN 0003-4916. doi: 10.1016/0003-4916(71)90108-4.

L. Landau and E. Lifshitz. *Mechanics*. Course of theoretical physics. Butterworth-Heinemann, 1976. ISBN 9780750628969.

G. Lindblad. On the generators of quantum dynamical semigroups. *Comm. Math. Phys*, 48:119–130, 1976.

S. Lloyd. Coherent quantum feedback. *Phys. Rev. A*, 62:022108, Jul 2000. doi: 10.1103/PhysRevA.62.022108.

Nallatech Limited. XtremeDSP Development Kit-IV User Guide. `URL: http://www.xilinx.com/support/documentation/boards_and_kits/ug_xtremedsp_devkitIV.pdf`, 2005.

R. J. Nelson, Y. Weinstein, D. Cory, and S. Lloyd. Experimental demonstration of fully coherent quantum feedback. *Phys. Rev. Lett.*, 85:3045–3048, Oct 2000. doi: 10.1103/PhysRevLett.85.3045.

H. Paik, D. I. Schuster, L. S. Bishop, G. Kirchmair, G. Catelani, A. P. Sears, B. R. Johnson, M. J. Reagor, L. Frunzio, L. I. Glazman, S. M. Girvin, M. H. Devoret, and R. J. Schoelkopf. Observation of high coherence in josephson junction qubits measured in a three-dimensional circuit qed architecture. *Phys. Rev. Lett.*, 107: 240501, Dec 2011. doi: 10.1103/PhysRevLett.107.240501.

E. M. Purcell. *Phys. Rev.*, 69:681, 1946.

D. Risté, C. C. Bultink, K. W. Lehnert, and L. DiCarlo. Feedback control of a solid-state qubit using high-fidelity projective measurement. *arXiv:1207.2944*, July 2012a.

D. Risté, J. G. van Leeuwen, H.-S. Ku, K. W. Lehnert, and L. DiCarlo. Initialization by measurement of a superconducting quantum bit circuit. *Phys. Rev. Lett.*, 109:050507, Aug 2012b. doi: 10.1103/PhysRevLett.109.050507.

C. Sayrin, I. Dotsenko, X. Zhou, B. Peaudecerf, T. Rybarczyk, S. Gleyzes, P. Rouchon, M. Mirrahimi, H. Amini, M. Brune, J.-M. Raimond, and S. Haroche. Real-time quantum feedback prepares and stabilizes photon number states. *Nature*, 477(7362):73–77, Sept. 2011. ISSN 0028-0836. doi: 10.1038/nature10376.

L. Steffen, M. P. da Silva, A. Fedorov, M. Baur, and A. Wallraff. Experimental monte carlo quantum process certification. *Phys. Rev. Lett.*, 108,:260506, Feb. 2012.

V. Steixner, P. Rabl, and P. Zoller. Quantum feedback cooling of a single trapped ion in front of a mirror. *Phys. Rev. A*, 72:043826, Oct 2005. doi: 10.1103/PhysRevA.72.043826.

R. Vijay, D. H. Slichter, and I. Siddiqi. Observation of quantum jumps in a superconducting artificial atom. *Phys. Rev. Lett.*, 106:110502, Mar 2011. doi: 10.1103/PhysRevLett.106.110502.

R. Vijay, C. Macklin, D. H. Slichter, S. J. Weber, K. W. Murch, R. Naik, A. N. Korotkov, and I. Siddiqi. Quantum feedback control of a superconducting qubit: Persistent rabi oscillations. *Nature*, 490:77–80, Oct 2012. doi: 10.1038/nature11505.

A. Wallraff, D. I. Schuster, A. Blais, L. Frunzio, R. S. Huang, J. Majer, S. Kumar, S. M. Girvin, and R. J. Schoelkopf. Strong coupling of a single photon to a superconducting qubit using circuit quantum electrodynamics. *Nature*, 431 (7005):162–167, 09 2004.

D. Walls and G. J. Milburn. *Quantum Optics*. Springer Berlin Heidelberg New York, 2008.

J. Wang and H. M. Wiseman. Feedback-stabilization of an arbitrary pure state of a two-level atom. *Phys. Rev. A*, 64:063810, Nov 2001. doi: 10.1103/PhysRevA.64.063810.

H. M. Wiseman. Quantum theory of continuous feedback. *Phys. Rev. A*, 49: 2133–2150, Mar 1994. doi: 10.1103/PhysRevA.49.2133.

H. M. Wiseman and G. J. Milburn. *Quantum Measurement and Control*. Cambridge University Press, 2009.

H. M. Wiseman, S. Mancini, and J. Wang. Bayesian feedback versus markovian feedback in a two-level atom. *Phys. Rev. A*, 66:013807, Jul 2002. doi: 10.1103/PhysRevA.66.013807.

Xilinx Inc. Virtex-4 FPGA User Guide. `URL: http://www.xilinx.com/support/documentation/user_guides/ug070.pdf`, 2008.

B. Yurke and E. Buks. Performance of cavity-parametric amplifiers, employing kerr nonlinearites, in the presence of two-photon loss. *J. Lightwave Technol.*, 24 (12):5054–5066, Dec 2006.

Acknowledgement

This thesis has been realized in the "quantum device lab" of Prof. Andreas Wallraff at ETH Zurich. I am deeply grateful to him that I was able to work on such an intriguing topic in my bachelor's thesis already.

Next I want to thank Christopher Eichler for supervising my work. In all the discussions we had he helped me concentrate on the essential aspects again and encouraged me to critically review past work.

I closely collaborated with Yves Salathé on the realization of the feedback experiment. His expertise in FPGA programming was invaluable to me. Even more than that, I appreciated his companionship during the experimental sessions.

Finally, I am thankful to all the rest of the team for the pleasant atmosphere. In particular Christian Lang, Lars Steffen and Matthias Baur readily helped me with all software related or technical problems.

Appendix A

Measurement and calibration procedure

In this section a brief summary of the experimental procedure is given that allows one to measure single shot and feedback histograms. This encompasses

1. a.c. Stark and dispersive shift
2. π pulse calibration via Rabi oscillations
3. exact qubit frequency via Ramsey
4. paramp calibration
5. phase calibration between measurement drive, pump and heterodyne LO

A.1 A.c. Stark and dispersive shift

First, system spectroscopy is conducted to find the transition frequencies $\omega_{r,g}$ of the resonator with qubit in the ground state and ω_{ge} of the qubit[1] ($g \leftrightarrow e$) together with their coupling strength g, qubit anharmonicity $\alpha = \omega_{gf}/2 - \omega_{ge} \approx -E_c/\hbar$ and resonator half width at half maximum κ.
Based on that, we measure the a.c. Stark shift $2\langle n\rangle\chi$ from qubit spectroscopy as a function of the measurement power $\propto \langle n\rangle$ (Figure A.1). This serves to calibrate the measurement power corresponding to one photon and to the critical photon number. For both calibrations the theoretical value of the dispersive shift χ from Equation 2.4 is used. Alternatively one can also determine χ from the frequency shift of the resonator if the qubit is continuously driven. For large qubit drive power saturation sets in and the bare resonator frequency $\omega_r = \omega_{r,g} + \chi$ is approached.

[1] The qubit transition frequency has to be tuned to the desired spot via magnetic flux.

In these measurements all microwave signals passed an up-conversion mixer modulated by an AWG for pulse generation such that it was not possible to sweep the generator output power P. Instead the output amplitude of the AWG was sweeped which leads to a calibration of the pulse amplitude $\propto \sqrt{P} \sim \sqrt{\langle n \rangle}$.
For all successive experiments we work with measurement powers corresponding to few photons (1 to 4) and the measurement frequency tuned to the bare resonator frequency ω_r.

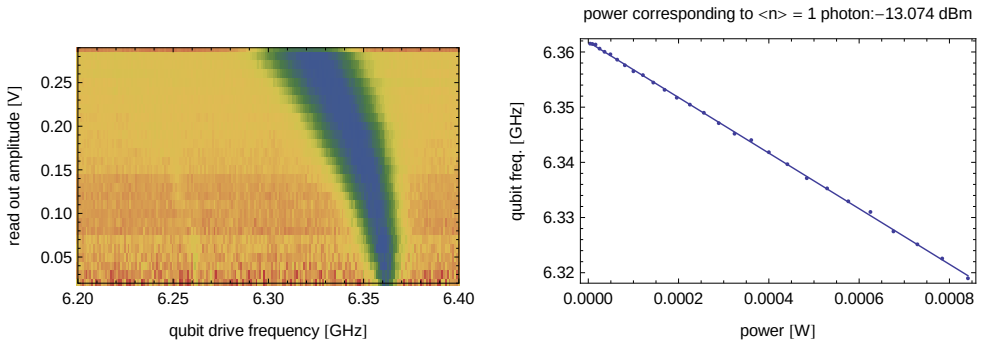

Figure A.1: A.c. Stark shift of the qubit $g \leftrightarrow e$ transition measured by varying the measurement pulse amplitude which leads to a quadratic dependence (**left**). Blue color indicates reduced transmission, orange represents unit transmission. On the **right** we plot the frequency shift versus read out power which gives linear dependence in excellent accordance with theory. From the slope the 1 photon power can be extracted.

A.2 Rabi pulse calibration

The next step is to calibrate the amplitudes for qubit π (and $\pi/2$) pulses at a given pulse shape. In these measurements Gaussian pulse envelopes with full width at half maximum or 15 ns were employed. To that end we record Rabi oscillations by increasing the amplitude of a qubit pulse (Figure A.2). The measurement pulse is positioned just after the Rabi pulse such that it does not distort the qubit frequency. The populations are determined via a fit to the solutions of the cavity Bloch equations (Equations 2.12 and 5.3). These amplitude calibrations are conducted with both AWG's Tektronix 5014 and Tektronix 520.
Additionally, the qubit relaxation time T_1 is obtained from measuring the qubit population in dependence of the delay between a Rabi π pulse and the read-out pulse (Figure A.3). At this step it should be reconsidered whether the qubit resonator detuning is appropriate for the feedback experiment in terms of T_1 and the read out SNR.

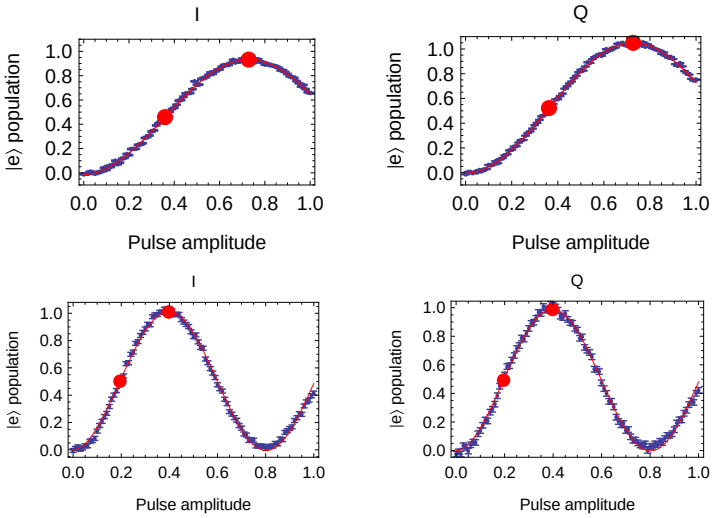

Figure A.2: Rabi oscillations of the qubit excited state population with pulses generated from the AWG Tektronix 5014 (top) and AWG Tektronix 520 (bottom). The pulse amplitude is given in units of V. The $\pi/2$ and π amplitudes for Rabi pulse calibration are marked by red dots.

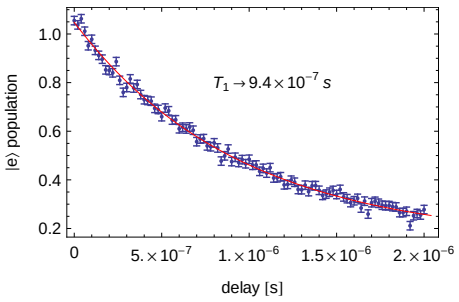

Figure A.3: Excited state population decay obtained from of a T_1 relaxation measurement.

A.3 Exact qubit frequency

Rabi pulses achieve maximal excitation of the qubit only if the detuning between the drive and the $g \leftrightarrow e$ transition frequency is zero. In order to establish this condition a Ramsey interference experiment is conducted. The qubit drive frequency is slightly detuned from the originally determined ω_{ge} (typically by 4 MHz) and the revival oscillations after two successive $\pi/2$ pulses are measured as a function of the inter-pulse delay. Since we work in a rotating frame at the qubit drive frequency this should simply reproduce the manually introduced detuning from the true qubit frequency (Figure A.4). Moreover the oscillations decay with the transverse relaxation time T_2. This experiment needs to be conducted with only one AWG. Afterwards the Rabi amplitudes need to be redetermined.

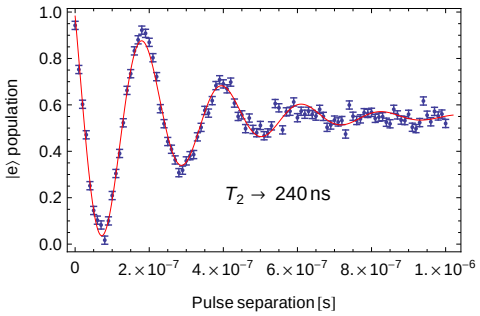

Figure A.4: Experimental Ramsey fringes that decay with T_2.

A.4 Paramp Calibration

Now that the qubit-resonator system is fully characterized, we turn to the paramp which has not been employed so far. Remind that phase sensitive amplification needs precise knowledge of the bare resonator frequency where all qubit state information is contained in a single quadrature of the transmitted field. Thus we need to *finally* set the measurement drive as well as the paramp pump to that frequency.

First the paramp is characterized by measuring its resonance (driven by the pump at moderate power) as a function of magnetic flux. After settling to a resonance frequency near the later working point and setting the pump frequency to the bare resonator frequency, gain and bandwidth are measured as a function of the pump power and the magnetic flux. This is achieved by adding a strongly attenuated (-60 dBm) test signal provided by a second mw generator.

At a point with moderate gain ($\sim$ 20 dB) and bandwidth ($\sim 10 - 20MHz$) and reasonable gain curve (Figure A.5), the residual pump signal leaving the paramp has to get cancelled such that only the true signal is observed. This cancellation procedure [Govenius, 2012] is realized by means of destructive interference with a coherently displaced and phase shifted branching of the pump (Figure A.6).

A.5 Phase calibration

After setting up the qubit-resonator and paramp systems separately we still need to synchronize the relevant phases of their drives (measurement tone and pump tone) in order to amplify the significant quadrature. We do so by sweeping the phase of the read-out tone, keeping the pump phase fixed, and thereby maximize the (averaged) state distances $|\alpha_e - \alpha_g|$ between ground (g) and excited (e) state responses. Here, $\alpha = I + iQ$. By keeping both qudratures, we can neglect the down-conversion LO phase in this step. Once the relative phase between read-out and pump phase is adjusted correctly (maximal state discrimination in both

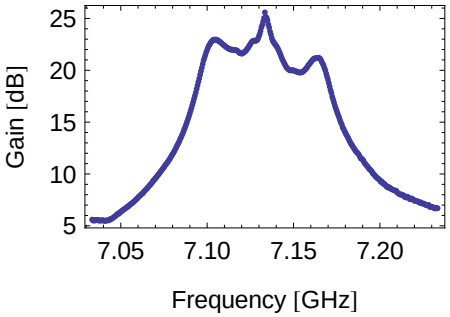

Figure A.5: The measured gain curve for the paramp settings used for the feedback experiments in this thesis. At $\sim$ 7.134 GHz there is a slight spike which might be due to imperfect pump displacement cancellation. This curve is rather inhomogeneous compared to an ideal Lorentzian possibly causing undesired noise properties. This has however not been further investigated.

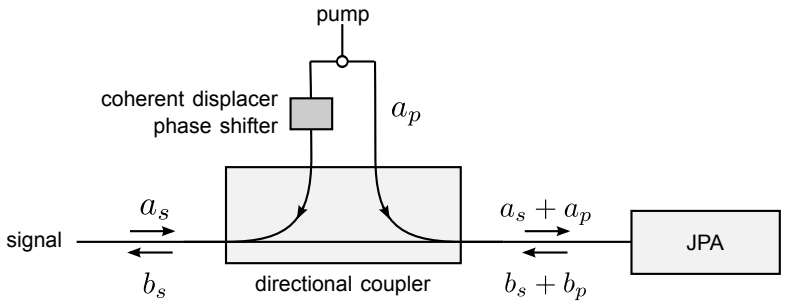

Figure A.6: Input and output of the Josephson parametric amplifier (JPA). The input modes are denoted a, the output or amplified modes b. The pump (p) is splitted into two parts in order to generate a cancellation signal (by coherent displacement and phase shifting) that destructively interferes with the residual pump signal. In the end the output originates exclusively from the signal (s) input.

quadratures), we can tune the LO phase such that all phase information is contained in the I quadrature only. This is the qudrature the FPGA looks at to make its state estimate.

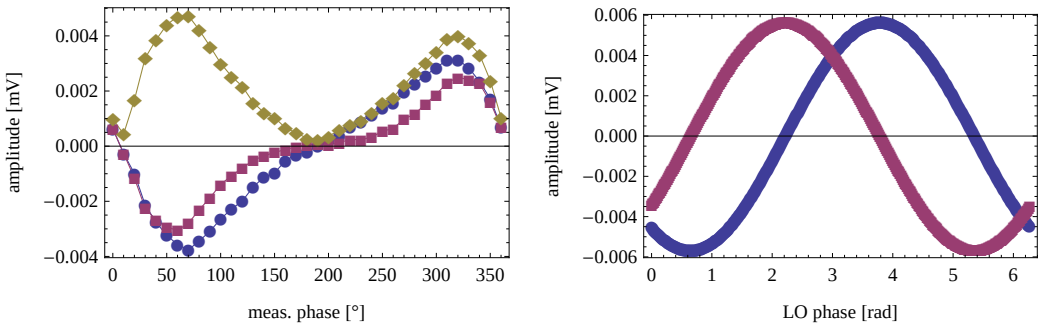

Figure A.7: Measured average distinguishability of ground and excited state while read out phase (left) and down-conversion LO phase (right) are sweeped in order to find the optimal positions. The time averaged distances between the pointer states in I quadrature (blue) and Q quadrature (red) are shown in both graphics. For the read out phase, maximal distinguishability refers to maximum of the absolute difference $|\alpha_e - \alpha_g|$ from both quadratures which is drawn in yellow.

Appendix B

FPGA feedback application

In this section, the relevant block diagrams of the feedback FPGA application which were created with the software *Simulink* by *MathWorks Inc.* are presented. This is not meant as a detailed description but rather as a list to complement the description in Section 4.3.2. The steps covered are, in the given order,

1. digital down conversion and filtering
2. digital signal processing and feedback loop
3. histogram address generation for storage on the RAM

Figure B.1 also provides an overview of the chronology of the signal processing in the FPGA.

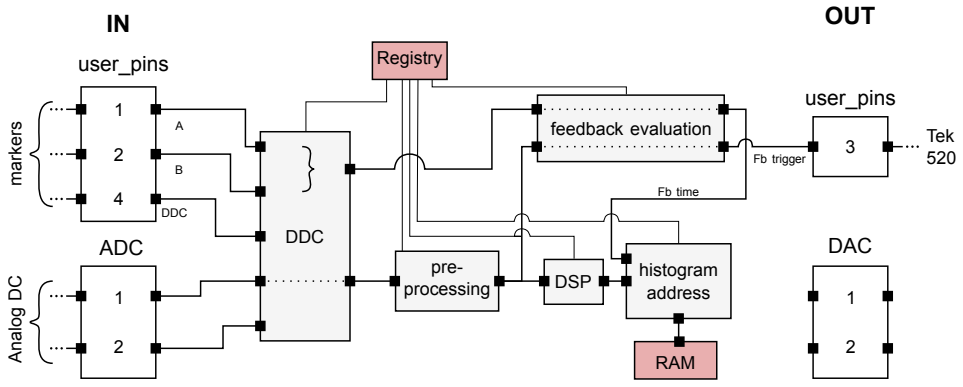

Figure B.1: A rough overview of the signal processing steps in the FPGA and their chronological order.

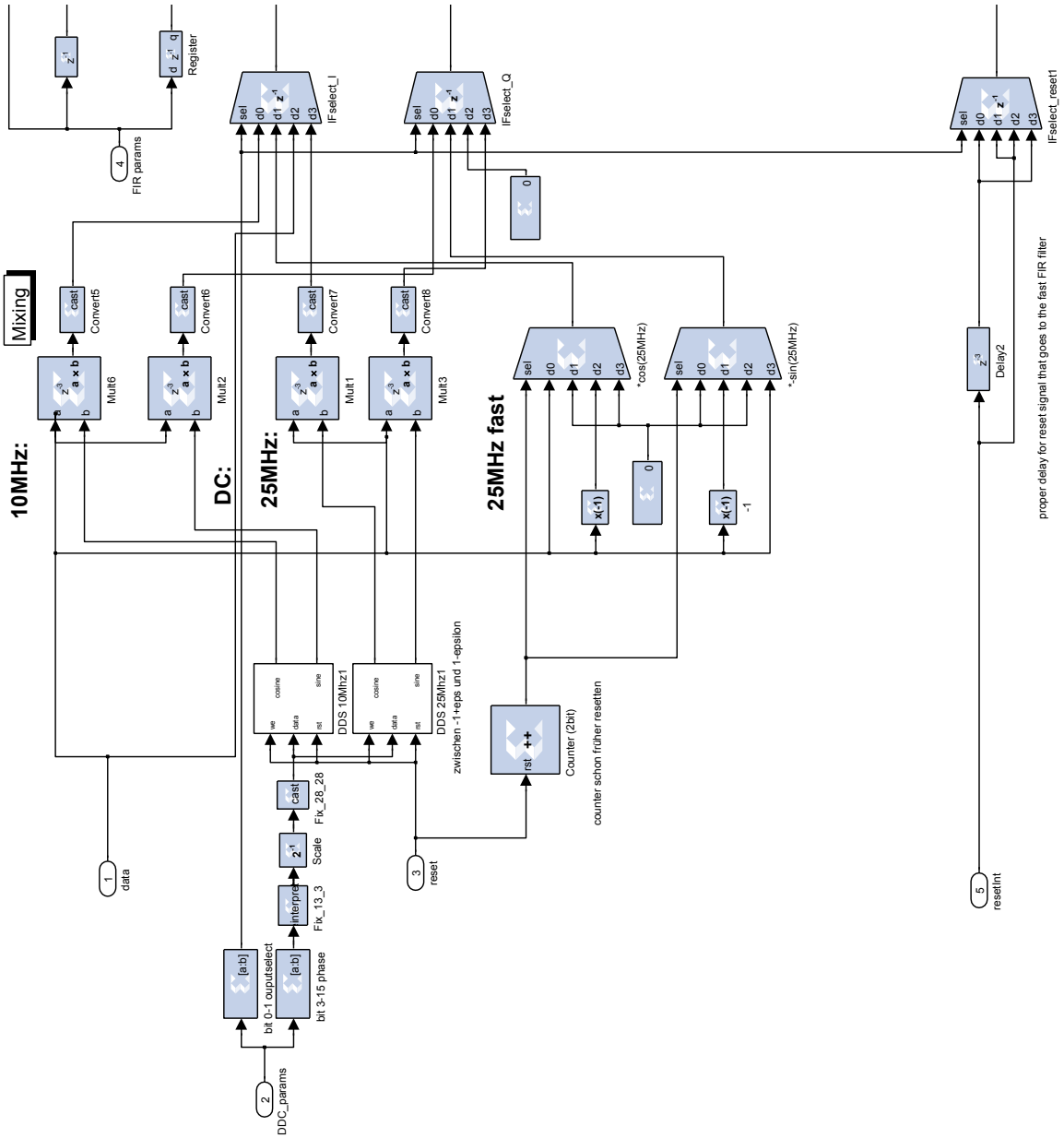

Figure B.2: Digital down conversion and filtering, part 1: digital down conversion.

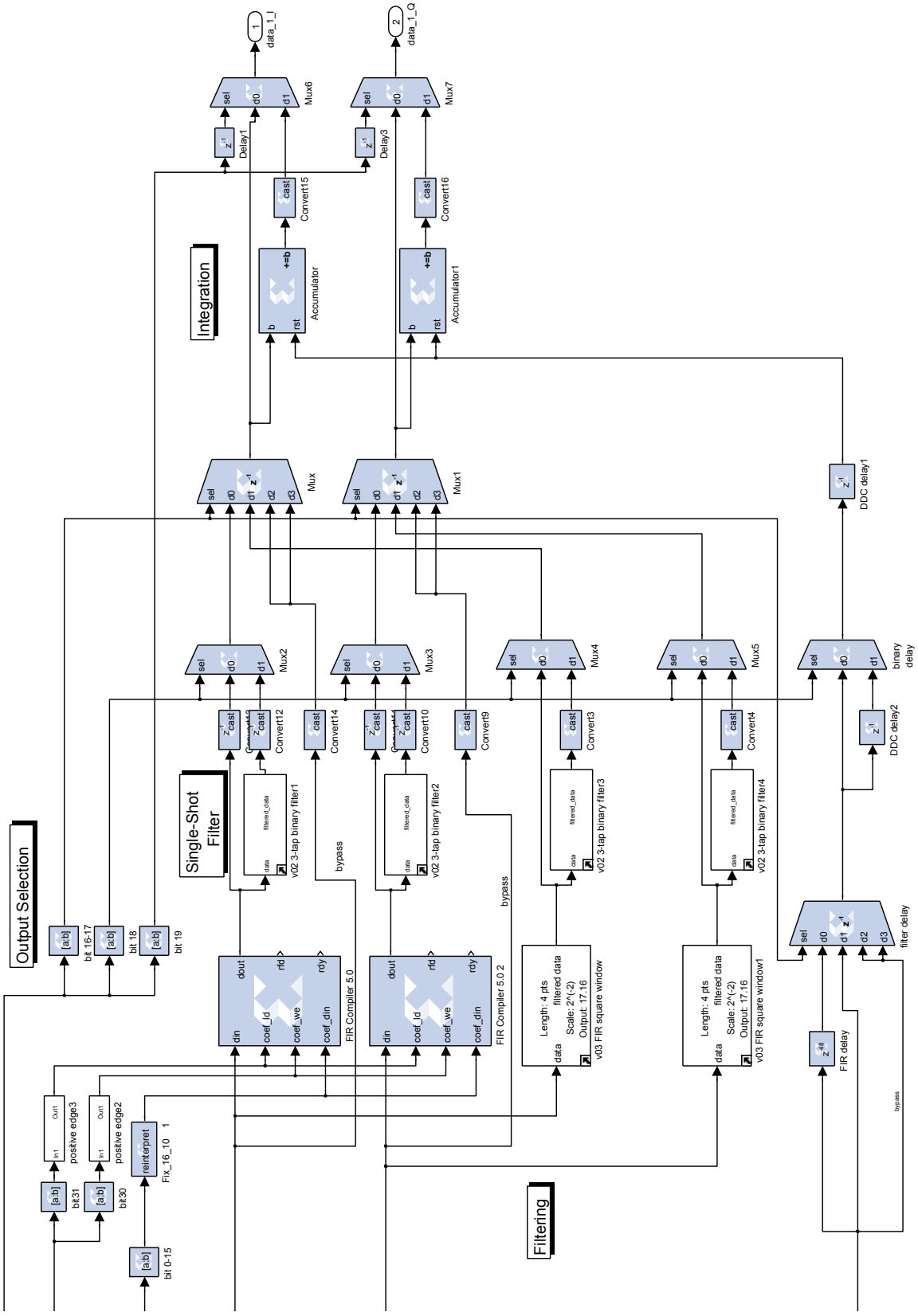

Figure B.3: Digital down conversion and filtering, part 2: filtering.

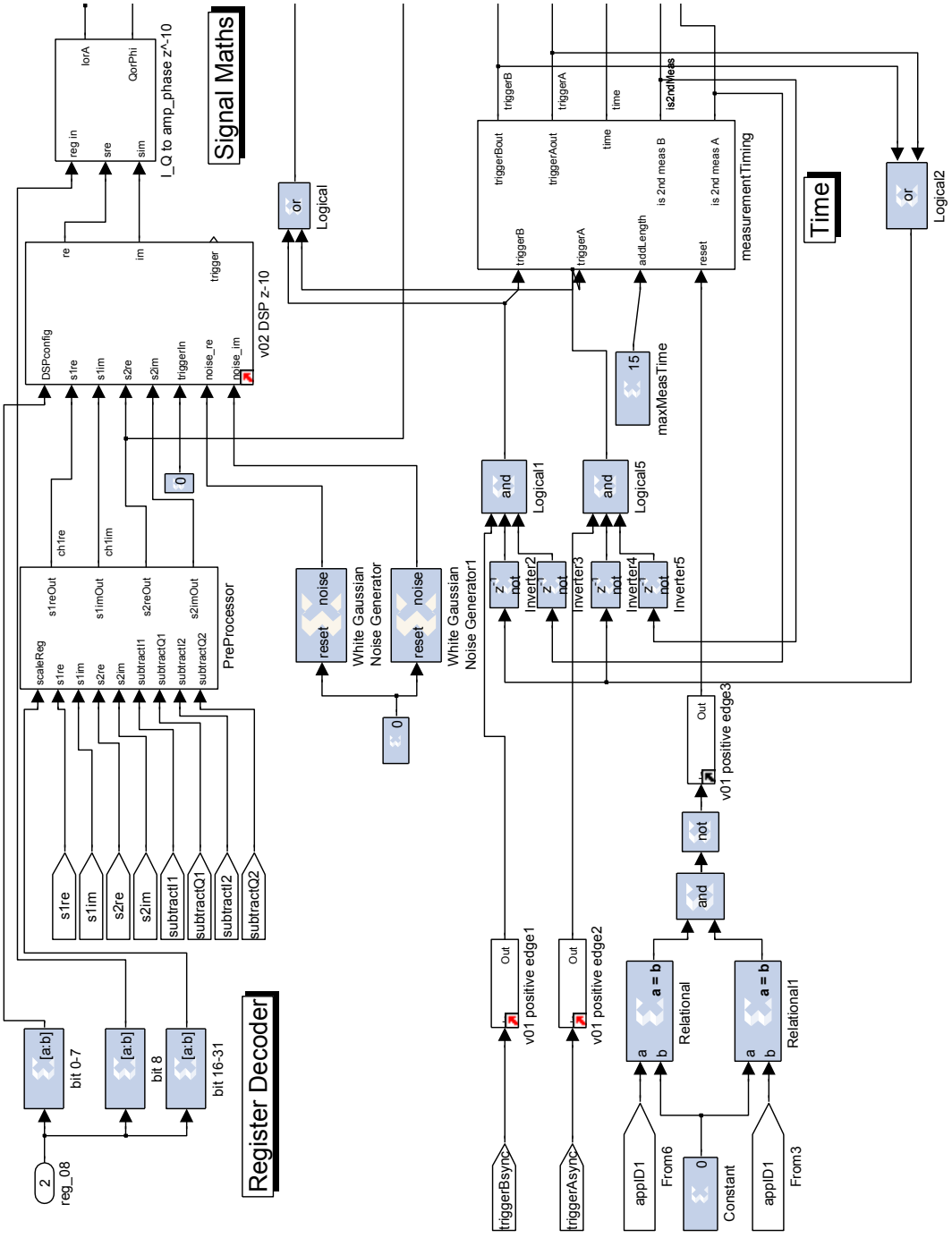

Figure B.4: Signal processing after digital down conversion and filtering, part 1.

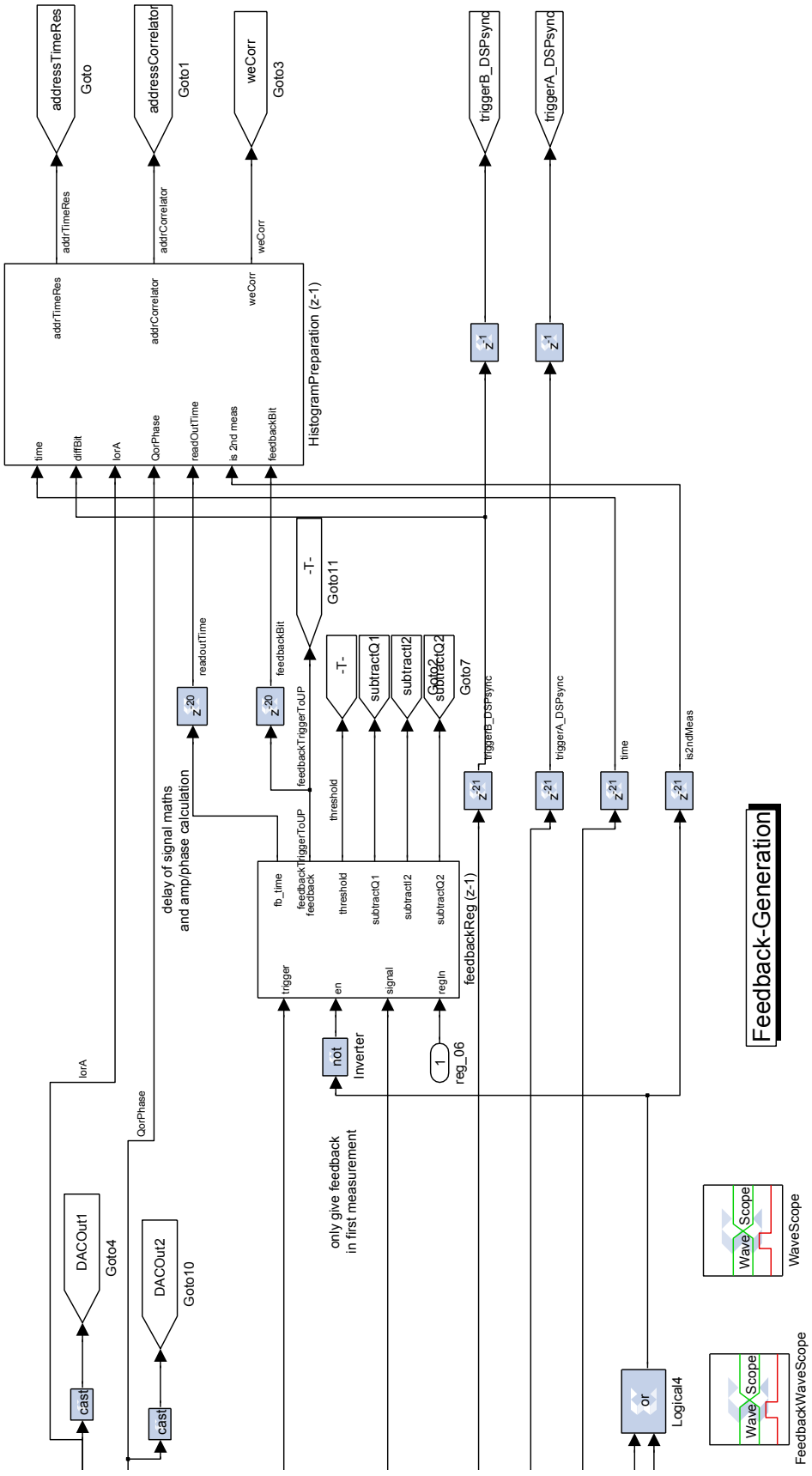

Figure B.5: Signal processing after digital down conversion and filtering, part 2.

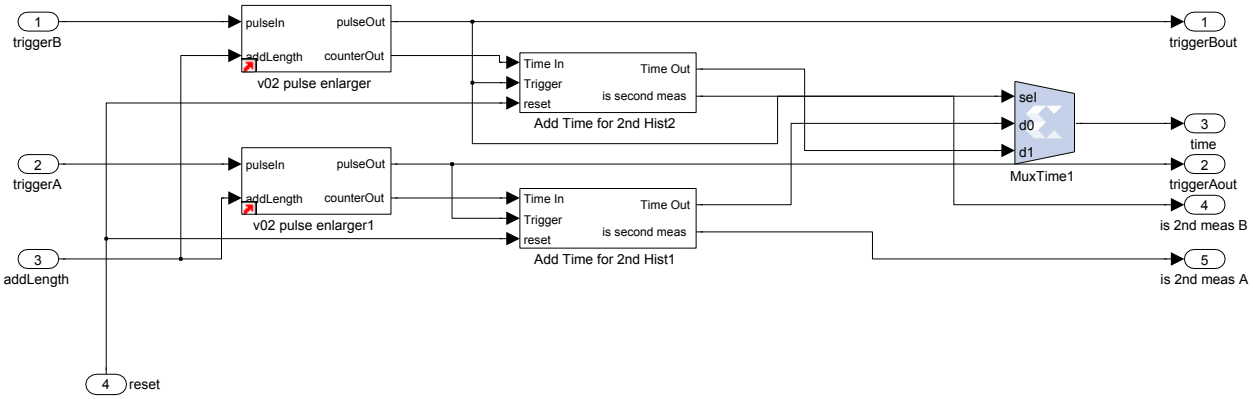

Figure B.6: Counting the time elapsed during the time windows starting with the incoming triggers for time resolved histograms.

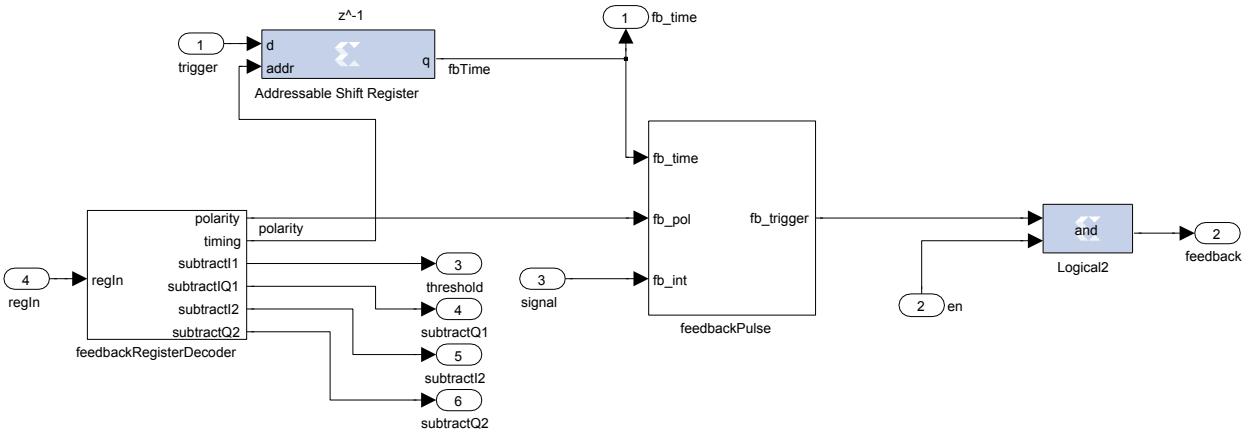

Figure B.7: Feedback register decoder and evaluation of the feedback condition

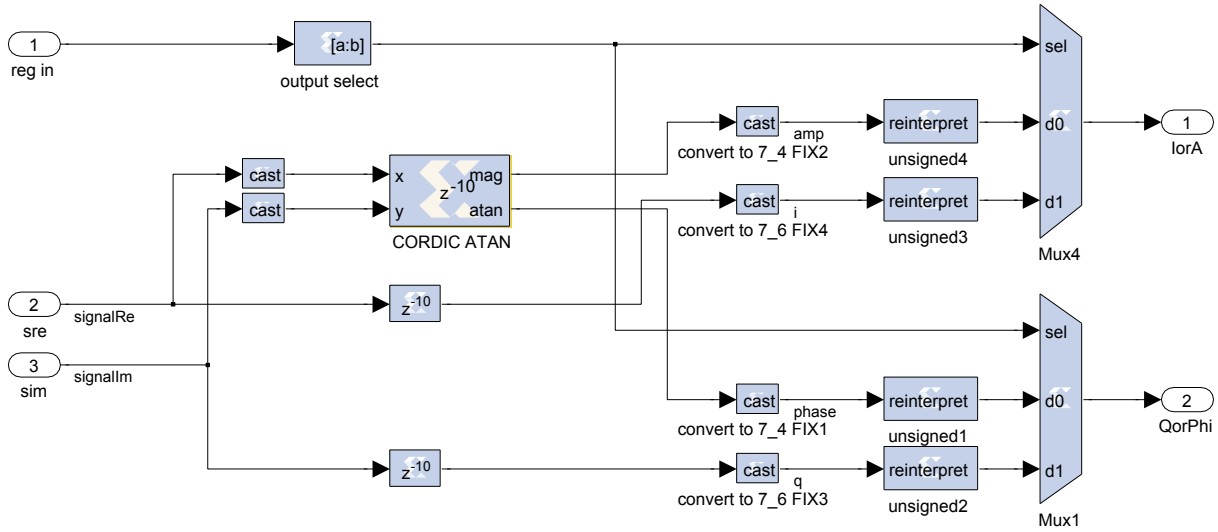

Figure B.8: Calculation of the polar representation (amplitude, phase) from the quadratures.

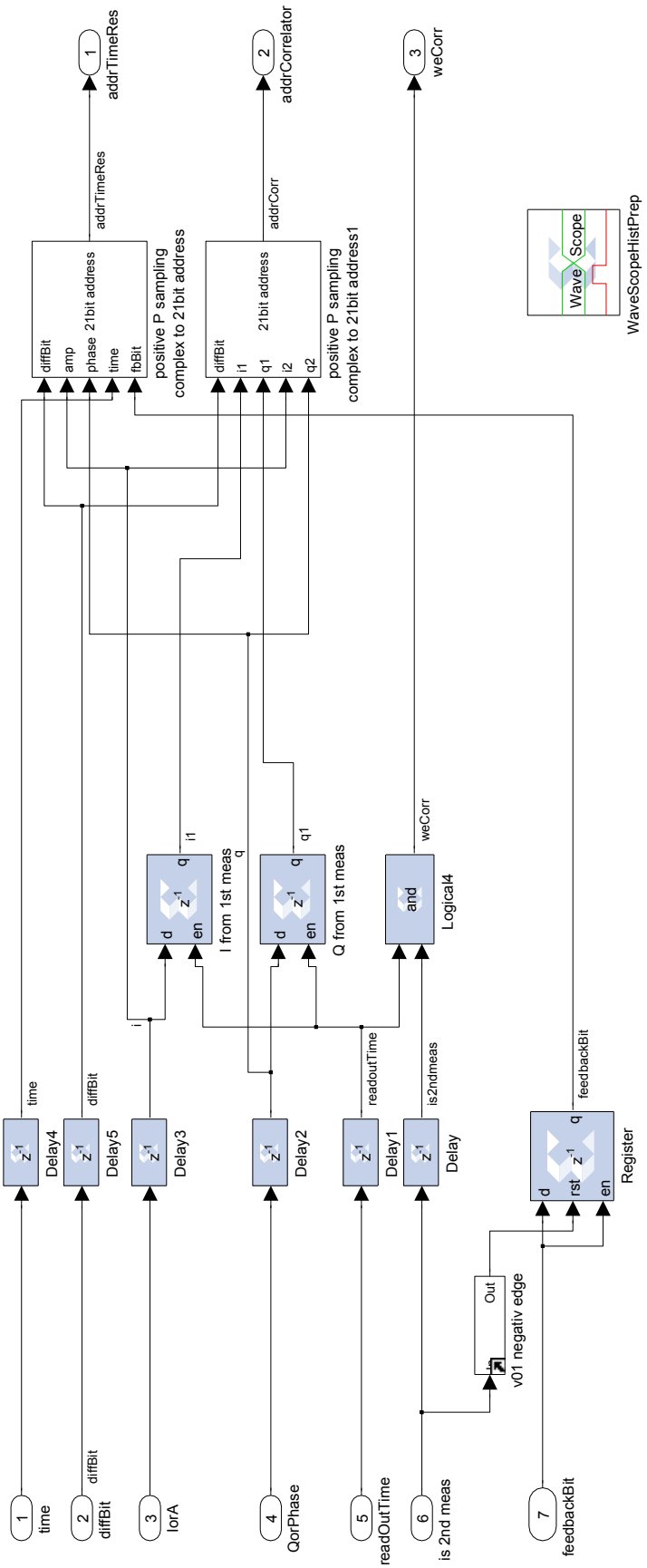

Figure B.9: Composition of the histogram address string.